NIH-PA Author Manuscript

NIH-PA Author Manuscript

NIH-PA Author Manuscript

NIH Public Access
Author Manuscript
Prog Mater Sci. Author manuscript; available in PMC 2011 June 27.

Published in final edited form as:
Prog Mater Sci. 2011 February ; 56(2): 139–174. doi:10.1016/j.pmatsci.2010.09.001.

Piezoelectric films for high frequency ultrasonic transducers in biomedical applications

Qifa Zhou[*], **Sienting Lau**, **Dawei Wu**, and **K. Kirk Shung**
NIH Resource Center for Medical Ultrasonic Transducer Technology, and Department of Biomedical Engineering, University of Southern California, Los Angeles, CA 90089, United States

Abstract

Piezoelectric films have recently attracted considerable attention in the development of various sensor and actuator devices such as nonvolatile memories, tunable microwave circuits and ultrasound transducers. In this paper, an overview of the state of art in piezoelectric films for high frequency transducer applications is presented. Firstly, the basic principles of piezoelectric materials and design considerations for ultrasound transducers will be introduced. Following the review, the current status of the piezoelectric films and recent progress in the development of high frequency ultrasonic transducers will be discussed. Then details for preparation and structure of the materials derived from piezoelectric thick film technologies will be described. Both chemical and physical methods are included in the discussion, namely, the sol–gel approach, aerosol technology and hydrothermal method. The electric and piezoelectric properties of the piezoelectric films, which are very important for transducer applications, such as permittivity and electromechanical coupling factor, are also addressed. Finally, the recent developments in the high frequency transducers and arrays with piezoelectric ZnO and PZT thick film using MEMS technology are presented. In addition, current problems and further direction of the piezoelectric films for very high frequency ultrasound application (up to GHz) are also discussed.

1. Introduction

1.1. Challenges of high frequency ultrasonic transducers

High frequency (HF) ultrasound is a promising imaging modality for providing a more detailed delineation of superficial anatomical structures, e.g., skin and eye or vascular structures via catheterization. Ultrasonic transducers with frequency higher than 30 MHz yield improved spatial resolution at the expense of a reduced depth of penetration. The resolution of ultrasound image is determined by the pulse bandwidth (axial resolution, R_{axial}) and the beam width (lateral resolution, R_{lateral}). Simple expressions for the ideal lateral and axial resolution of a focused transducer within the focal zone are given by:

$$\text{Axial resolution}(-6\ \text{dB}):\ R_{\text{axial}}=\frac{\lambda}{2BW}=\frac{c}{2f_cBW} \tag{1.1}$$

$$\text{Lateral resolution}:\ R_{\text{axial}}=\lambda F\#\frac{c}{f_c}F \tag{1.2}$$

© 2010 Elsevier Ltd. All rights reserved.

[*]Corresponding author. qifazhou@usc.edu (Q. Zhou).

NIH-PA Author Manuscript

NIH-PA Author Manuscript

NIH-PA Author Manuscript

where c is the speed of sound in the medium, f_c the center frequency of the transducer, BW the bandwidth of the transducer, $F\#$ the f-number (the ratio of focal distance to aperture dimension) and λ the wavelength. Thus, for a fixed number of cycles per pulse, an increase in frequency would result in a reduction in wavelength and pulse duration (increase in BW). If the transducer frequency is increased to 50 MHz, an axial resolution and lateral resolution of better than 25 μm and 60 μm for an f-number of 1.9 and bandwidth of 65% can be achieved respectively. However, at the same time, the penetration depth of ultrasound into the tissue must be sacrificed due to frequency-dependent attenuation. At 50 MHz, the depth of penetration for most tissues would be approximately to 8–9 mm.

HF single element transducers have been widely used in ultrasound imaging systems. However, mechanical scanning of a single element transducer shows poorer resolution out of focal zone and has limited frame rate. These problems can be overcome by adopting linear arrays, in which an image is formed by electronically sweeping a beam. Fabrication of high frequency ultrasonic linear arrays has remained a challenge following more than a decade of study. The task is even more difficult to build arrays at a frequency greater than 50 MHz which requires very small kerfs and thinner ceramic sheets [9]. Recent research has shown that micro-machining technology is a possible solution to such high-frequency applications although much improvement still needs to be made [10–12]. Piezoelectric films have already been widely used to fabricate micro-scale devices [1–8,13–15]. Among them, PZT thick film has been shown to exhibit good dielectric and piezoelectric properties, making it a possible ultrasonic transducer material candidate for high-frequency applications via micro-machined technology.

To date, there are a number of groups that have successfully fabricated PZT thick films for transducer applications. Tsuzuki et al. [16] prepared PLZT thick films by multiple electrophoretic deposition and sintering process. Barrow et al. [17] and Lukacs et al. [18] have reported thick PZT ceramic coatings using sol–gel derived porous 0–3 composites for high frequency transducer application. High frequency ultrasound array transducers using piezoelectric thin films on larger structures are being developed for high-resolution imaging systems by Trolier-McKinstry et al. [10]. In their work, metal-oxide semiconductor (CMOS) transceiver chip for a 16-element array was fabricated with ultrasound front-end chip containing beam-forming electronics and receiver circuitry. In addition, Dausch et al. reported the design and fabrication of 2D pMUT arrays [19]. They also described the vibrational modes for operation of flexure-mode pMUT elements, transmit output pressures, receive and pulse-echo characteristics, and B-mode imaging performance of the 81-element 2D arrays at a center frequency of approximately 7 MHz [20]. Despite above progress the improving quality of piezoelectric films and exploring optimum process for high frequency transducers are still challenge.

1.2. The scope of this review

In this review, we focus on the design, fabrication and application of piezoelectric thick films for high frequency ultrasonic transducers in biomedical imaging application. Recent progress in the development and application of ultrasonic transducers is presented and the challenges in pushing the transducers/arrays to higher operating frequency (>100 MHz) are addressed. Section 2 gives the basic principles of piezoelectric effect. Section 3 reviews the important design issues for ultrasonic transducer. Section 4 addresses piezoelectric films for high frequency ultrasonic transducer application. Section 5 presents fabrication and characteristics of high frequency piezoelectric films transducers. The current problems and future direction for very high frequency transducer applications in the near future are also addressed.

NIH-PA Author Manuscript
NIH-PA Author Manuscript
NIH-PA Author Manuscript

2. Basic principles of the piezoelectric effect

The piezoelectric effect was first reported by the Curie Brothers in 1880 [20]. The original discovery, that polarization charges are induced in response to an external mechanical stress, is known as direct piezoelectric effect. The converse piezoelectric effect refers to a dimensional change resulted from an applied electric field. Natural piezoelectric crystals, such as quartz and tourmaline, are seldom used today as transducer materials in diagnostic ultrasonic imaging due to their weak piezoelectric properties. The most popular piezoelectric material is the polycrystalline ferroelectric ceramic materials, such as barium titanate ($BaTiO_3$) and lead zirconate titanate (PZT), which consist of randomly orientated crystallites (grains), separated by grain boundaries. These materials are much less expensive than single crystals but offer strong piezoelectric properties along polarization axes. Poling of a ferroelectric material can be carried out at room temperature or by heating it to a temperature just above the Curie temperature of the material and then allowing it to cool slowly in the presence of a strong electric field, typically in the order of 20 kV/cm, applied in a direction in which the piezoelectric field is required. The electric field is usually applied to the material by mean of two electrodes. This occurs due to the presence of so-called ferroelectric domains (regions with different orientations of the spontaneous polarization) in a sintered ferroelectric ceramic. The boundaries between ferroelectric domains (often called domain walls) can move under the action of an applied field, so that the spontaneous polarization can be reoriented in the crystallographic direction closest to the field direction. As a result of such poling process, an initially macroscopically centrosymmetric ceramic material loses the inversion center and becomes piezoelectric.

For single crystals, a plate cut with its surface perpendicular to the x-axis of a crystal is called x-cut, and so forth. The crystallographic axes, x, y, and z are also sometimes represented by numbers 1–3. Unlike single crystals which have crystallographic axes, the principle axis, z, of a ferroelectric ceramic is defined as the direction in which the material is polarized [21]. A piezoelectric strain constant, d_{33}, represents the strain produced in the z direction by applying an electric field in the z direction and d_{31} is the strain in the x direction produced by an electric field in the z direction when there is no external stress. Here it is important to note that the effective properties of a material such as electromechanical coupling factor k depends upon boundary conditions and therefore upon the shape of the material. Taking PZT piezoceramic as an example, for thin plate, the factor k_t is about 0.5; for a long bar, the factor k_{33} is about 0.7.

For a thin film deposited on a rigid substrate, the actual piezoelectric response of the films is quite different from that of the bulk ceramics. The films are laterally clamped by the substrates and thus cannot vibrate freely. The effective piezoelectric coefficients subjected to the clamping are related to the bulk ceramic values by [22,23]:

$$d_{33,f}=d_{33}-\frac{2s_{13}^{E}}{s_{11}^{E}+s_{12}^{E}}d_{31} \tag{2.1}$$

$$e_{31,f}=\frac{d_{31}}{s_{11}^{E}+s_{12}^{E}}=e_{31}-\frac{c_{13}^{E}}{c_{33}^{E}}e_{33} \tag{2.2}$$

where s_{ij} and c_{ij} represent component of the elastic and stiffness tensor, respectively. The practical effect is that the $d_{33,f}$ and $e_{31,f}$ coefficients are smaller than the bulk values (note that the absolute value of $e_{31,f}$ is higher than e_{31}).

NIH-PA Author Manuscript NIH-PA Author Manuscript NIH-PA Author Manuscript

3. Design considerations of the ultrasonic transducer

3.1. Basic principles

The simplest ultrasonic transducer is single-element piston transducer (Fig. 1), which is based on a piezoelectric plate or disc poled along the thickness direction and used in its thickness mode, so its thickness t defines the resonance frequency f of the device given by [24]:

$$t = n\frac{c_p}{2f} \tag{3.1}$$

with the lowest resonant frequency being $n = 1$, where n is an odd integer, and c_p the acoustic wave velocity in the piezoelectric material. When an electrical impulse is applied to the plate, and an acoustical resonance is induced, which will lead to the generation of pressure waves (a and b as labeled in Fig. 1) with opposite directions at the front and rear surfaces of the element. Since the plate, typically a piezoceramic, has higher acoustic impedance (~33 MRayl) than that of biological tissue or water (~1.5 MRayl), reverberation of acoustic waves in the plate will cause considerable after-ringing, lengthening the duration of an acoustic pulse. Thus, a piezoceramic plate alone would lead to a very poor axial resolution. Therefore, if desired, two other layers may be added to active layer to reduce the ringing. One is known as front matching layer for improving the energy transmission between the active layer and load medium. The rear layer is oftentimes a thick backing, which not only serves as a mechanical support for the active element, but also allows acoustic energy flowing into it to be absorbed if necessary, thus damping out the reverberation. The selection criteria of these mechanical layers are presented in next section.

Various sophisticated one-dimensional circuit models exist to stimulate the behavior of the transducer including the Mason model, Redwood model and KLM model [25]. Among them, the KLM is more physically intuitive. The effects of matching layers and backing material can be readily included as sections of transmission lines. This model divides a piezoelectric element into two halves, each represented by an acoustic transmission line. The acoustic transmission line serves as a secondary circuit, which is linked with an electric primary circuit by an ideal transformer as shown in Fig. 2.

The component and constant used in the model are list below:

$$C_o = \frac{\varepsilon_{33}^S A}{t} \tag{3.2}$$

$$k_t^2 = \frac{e_{33}^2}{c_{33}^D \varepsilon_{33}^S} \tag{3.3}$$

$$\omega_o = \frac{2\pi c_p}{d} \tag{3.4}$$

$$\Phi = k_t \sqrt{\frac{\pi}{\omega_o C_o Z_c}} \mathrm{sinc}\left(\frac{\omega}{2\omega_o}\right) \tag{3.5}$$

$$C' = -\frac{C_o}{k_t^2}\left(\mathrm{sinc}\left(\frac{\omega}{\omega_o}\right)\right)^{-1} \tag{3.6}$$

where A, transducer area; t thickness of the piezoelectric material; ρ, density of the piezoelectric material; c_p, the speed of sound in the piezoelectric material; Z_c, acoustic impedance of the piezoelectric layer ($=\rho c_p$); ε_{33}^S, clamped dielectric permittivity; e_{33}, piezoelectric constant; c_{33}^D, elastic constant of piezoelectric layer; ω_o, resonant frequency.

With the KLM model, the electric impedance of the transducer is given as

$$Z_{in} = \frac{1}{j\omega C_o} + \frac{1}{j\omega C'} + \frac{Z_1 Z_2}{(\Phi^2(Z_1+Z_2))} \tag{3.7}$$

where Z_1 and Z_2 are the input impedances of the acoustic transmission line looking towards the front acoustic port and back acoustic port, respectively. Equations that describe insertion loss and pulse-echo response can also be obtained with the KLM model. From the design point of view, the KLM model allows an intuitive approach to be used in optimizing the transducer performance: the two acoustic ports can be used to interpret front matching and rear backing; the electrical port, on the other hand, can be used to explain electrical matching. The transducer stimulation software PiezoCAD, based on this model, has been extensively used in transducer design.

3.2. Mechanical matching

For medical ultrasound imaging applications, a transducer with a broad bandwidth and low loss is preferred. Mechanical matching, which includes front matching and rear backing, is a well-established solution to improve the performance of ultrasonic transducers. When a single electrical pulse is applied across the piezoelectric element, pressure waves (a and b as illustrated in Fig. 3.1) will be generated in the front and back directions. The pressure wave *b* moves forward and reaches the front surface of the piezoelectric element. The pressure transmits into the front loading medium at a normal incidence is governed by the transmission coefficient:

$$T = \frac{2Z_l}{Z_p + Z_l} \tag{3.8}$$

where Z_l and Z_p are acoustic impedance of the loading medium and piezoelectric element, respectively. With the typical values (Z_l ~ 1.5 MRayl for water and Z_p ~ 33 MRayl for piezoceramic material), the transmission coefficient T is calculated to be only around 10%. Therefore, a matching layer may be inserted in between piezoelectric layer and the loading medium to compensate for their acoustic impedance mismatch. Using transmission line theory, 100% transmission occurs when thickness of the matching layer is close to $\lambda_m/4$ (λ_m

NIH-PA Author Manuscript NIH-PA Author Manuscript NIH-PA Author Manuscript

NIH-PA Author Manuscript

is the wavelength in the matching material) and acoustic impedance of the matching material Z_m satisfies [26]

$$Z_m=(Z_pZ_l)^{1/2} \tag{3.9}$$

Using the KLM model, Desilets et al. [27] also determined that the optimum impedance of the matching layer(s) for pulse excitation should be modified to

$$Z_m=(Z_pZ_l^2)^{1/3} \tag{3.10}$$

To facilitate improved front matching, sometimes, two or more quarter-wavelength matching layers may be used. If two matching layers are used, the acoustic impedance of these layers can be determined by [27]

$$Z_{m1}=(Z_p^4Z_l^3)^{1/3} \tag{3.11}$$

$$Z_{m2}=(Z_pZ_l^6)^{1/7} \tag{3.12}$$

To further increase the transducer performance, a double $\lambda/8$ matching scheme has been proposed. Theoretically, two $\lambda/8$ matching layers are equivalent to a single quarter matching layer and works as a simplified graded matching. This kind of simplified graded matching can improve the transducer bandwidth with proper selection of backing material as demonstrated by Lau et al. [28].

Similarly, when the pressure wave *a* moves backward and hits the rear surface of the piezoelectric element at a normal incidence, a fraction of energy will be transmitted into the air and the rest is reflected back and is governed by the reflection coefficient:

$$R=\frac{Z_a-Z_p}{Z_a+Z_p} \tag{3.13}$$

where Z_a is the acoustic impedance of air, which is close to zero. It is obvious that a majority of the energy will be reflected back to the front face. In reality, even with matching layers, 100% transmission is impossible at the front surface. The reflected wave thus will reverberate inside the piezoelectric element, causing a long ring down (narrow bandwidth) of the produced ultrasonic pulse. Backing, therefore, is used to damp out the ringing due to acoustic impedance mismatch between the air and piezoelectric materials. Ideally, when the acoustic impedance of the backing (Z_b) is equal to the piezoelectric element (Z_p), there will be no reflection ($R = 0$) and a monocycle pulse can be generated. However, the sensitivity will be significantly reduced in this case. A compromise has to be made between bandwidth and sensitivity in practical applications.

In contrast to conventional low-frequency (below 10 MHz) devices, numerous issues must be addressed in the use of matching layers for high frequency transducers. First, the ability

NIH-PA Author Manuscript NIH-PA Author Manuscript NIH-PA Author Manuscript

to fabricate ultra-thin layers is problematic with the projected thickness tolerances on the order of a few microns; secondly the issue of scale, i.e. specifically for composites where the layer is on the order of the microstructural features giving rise to acoustic non-homogeneity and scattering; and thirdly, the intrinsic increase in attenuation with increasing frequency. According to Eqs. (3.10)–(3.12), materials with acoustic impedances ranging between 2 and 10 MRayl are desired for single and double-layer matching scheme. The state of the art to produce matching layers with adjustable acoustic impedance is to mix micro- or nano-scale powders, such as Al_2O_3, CeO_2 and Ag, in polymer and to adjust the acoustic impedance by the content of powder [29–31]. Proper selection of the particle size can minimize the scattering effect at high frequencies.

For the backing material, conductive epoxy, E-solder 3022 (Von Roll Isola Inc., New Haven, CT) has been used [32]. This material has a high attenuation (120 dB/mm at 30 MHz) and relatively low acoustic impedance (5.9 MRayl), making it possible to achieve low insertion loss, short and well-shaped pulses suitable for imaging purpose if optimal matching is achieved in the front. Tungsten loaded epoxy is another popular choice [28,33]. It has higher acoustic impedance ranged from 8 to 20 MRayl by varying the content of Tungsten and is used when the broad bandwidth is the priority consideration. Besides being lossy, the backing materials are usually rigid so as to support the fragile active elements.

3.3. Electrical matching

Transducers are often electrically tuned to maximize energy transmission (reduce insertion loss or enhance relative pulse-echo sensitivity) and/or improve their bandwidth. Ideally, for maximal energy transmission, the transducer input impedance should be real (tune out the clamped capacitance) and the input resistance should match the electrical impedance of the source (normally 50 Ω in termination). The capacitance can be tuned out by simply adding an inductor either in series or in parallel with the transducer [27,34]. It can be calculated that at series resonance (f_r) a shunt inductor with a value of $1/(\omega_r^2 C_o)(C_o = \varepsilon_{33}^S A/t$, where A and t are the surface area and thickness of the transducer element, respectively) may be used (see Fig. 3a). For the parallel resonance (f_a) case, a shunt inductor with a value of $1/(\omega_a^2 C_o) + R_a^2 C_0$ (where $R_a = 4k_t^2 Z_c / \pi\omega_a C_0 (Z_1 + Z_2)$, Z_1 is acoustic impedance of load medium, Z_2 is acoustic impedance of the backing material and ω_a is parallel resonance frequency) can be used (see Fig. 3b). To match the resistance to source impedance, a transformer may be used. Hunt et al. [35] suggested that the closer the transducer's resistance is to 50 Ω before transformer tuning, the better the transducer's bandwidth is after transformer tuning.

4. Materials for high frequency ultrasonic transducers

4.1. Specific material parameters for transducer design

In transducer design, there are several material properties such as elastic, dielectric, piezoelectric constants, and machinability in addition to cost that have to be considered. Two of the most important material parameters for fabrication of medical ultrasound transducers are the electromechanical coupling coefficient (k) and acoustic impedance (Z_a). The k factor indicates the capability of the material to convert electrical energy into mechanical energy and vice versa. Its value ranges from 0% to 100%, and it should be as high as possible. The k factor depends not only on the material properties but also on the material geometry. A few important material geometries are frequently used in ultrasonic imaging as shown in Fig. 4. For a large plate or disc with the lateral dimension(s) much larger than the thickness, the thickness mode electromechanical coupling coefficient, k_t, is used. For a bar or pillar with the lateral dimensions much smaller than the thickness, the factor of interest is k_{33}. For intermediate cases (one small and one large lateral dimensions

with a thickness value between them), the $k_{33}^{'}$ is frequently used for linear array element. (Note: $k_{33}^{'}$ is named k_{33}^{w} in the IEEE standard for piezoelectricity [36].) All these k values can be written in terms of material constants, and the corresponding formulas are derived based on certain one dimensional (1D) approximations without considering the cross coupling with lateral modes. The prerequisite is that the designed dimension of the desired mode must be much larger or smaller that other dimensions. In practical construction of high frequency transducer array, the array element height is determined by the operating frequency and the element lateral size is also constrained by the wavelength, thus element dimensions may not satisfy the 1D approximation. To address this problem, Kim and his co-workers [37–39] employ the theory for two-dimensional coupled vibrations and also consider the strain vibrations with aspect ratio in formulating the unified expression. This unified formula, Eq. (4.1), can be used to calculate the electromechanical coupling coefficient for a rectangular slender bar array element of any aspect ratio [37].

$$k=\frac{\left[\frac{1+\sigma}{1+\sigma}(g^2(G)-1)\frac{s_{13}^E}{s_{11}^E}d_{31}+\left(d_{33}-\frac{s_{13}^E}{s_{11}^E}d_{31}\right)\right]}{\sqrt{\left[\frac{1+\sigma}{1+\sigma}(g^2(G)-1)\frac{(s_{13}^E)^2}{s_{11}^E}\right]\left[\frac{1+\sigma}{1+\sigma}(g^2(G)-1)\frac{d_{31}^2}{s_{11}^E}+\left(\varepsilon_{33}^T-\frac{d_{31}^2}{s_{11}^E}\right)\right]}} \tag{4.1}$$

The acoustic impedance, defined as the ratio of acoustic pressure p to particle velocity v in a given media, for a fluid is given by

$$Z_a=\frac{p}{v}=\rho c \tag{4.2}$$

where c is the acoustic wave velocity and ρ the density of the medium. It has a unit of kg/ m^2-s or Rayl. To achieve good energy transmission, the acoustic impedance of piezoelectric materials should be as close as possible to that of the propagating medium, i.e. biological tissues for imaging or water for pulse-echo testing; both have an acoustic impedance of ~1.5 MRayl. Many different piezoelectric materials are available to choose from when designing a single element or array transducer. Frequently used materials include piezoceramics, piezoelectric polymers and single crystals. The material properties for a few important piezoelectric materials are listed in Table 1. A critical look at the piezoelectric and acoustic properties of these materials in the interest of a certain application can greatly narrow down the choices.

4.2. Piezoelectric materials used in ultrasonic transducers and arrays

For large area high frequency devices, such as single or dual element transducers, a low dielectric constant allows better electrical matching to the electronics as previously discussed. Piezoelectric polymers such as polyvinylidene (PVDF) and its copolymer with trifluoroethylene (TrFE) have also been found to be useful for producing high frequency transducers [47,48]. After the processes of polymerization, stretching and poling, a thin sheet of PVDF with thickness ranging from 5 to 25 μm can be used as a transducer material. PVDF possess a high degree of flexibility, low density, and low acoustic impedance (4 MRayl) which facilitates impedance matching with media like water and biological tissues. Transducers made with this material are typically very wideband. However, due to its low electromechanical coupling coefficient (see Table 3.1), PVDF is not an ideal transmitting material. It however does have a low dielectric constant and a fairly high receiving constant.

NIH-PA Author Manuscript NIH-PA Author Manuscript NIH-PA Author Manuscript

NIH-PA Author Manuscript

NIH-PA Author Manuscript

NIH-PA Author Manuscript

Miniature PVDF hydrophones are commercially available with operating frequency up to 100 MHz. In case of P(VDF–TrFE), when the VDF content is within the range of 0.6–0.82, the material forms the polar β-phase directly from the melt [49]. Unlike PVDF, it can be polarized directly by applying an electrical field at elevated temperatures. This material exhibits a higher electromechanical coupling coefficient (k_t ~ 0.27–0.30) [50], and therefore has proven to be useful in the production of simple, high frequency single element and annular array transducers.

Alternatively, polycrystalline ferroelectric ceramic materials such as lead zirconate titanate, $Pb(Zr, Ti)O_3$ or PZT, have been the dominant materials for the active elements of transducers and arrays [51–56]. By adjusting the compositions close to morphotropic phase boundary (MPB), these ceramics possess very strong piezoelectric properties (k_t of ~0.5 and d_{33} value ranged from 100 to 600 pC/N), a wide range of relative permittivity ($\varepsilon_{33}^{T}/\varepsilon_o \sim 500 - 2400$) and low electrical and mechanical losses. Certain piezoelectric properties of PZT can be enhanced by doping. As a result, many types of PZT-based piezoceramics are available on the market. However, conventional piezoceramics, having grain sizes in the order of 5–10 μm, are not particularly suitable for high frequency transducer applications, where the dimensions of the active elements can be on the order of tens of micrometers. For example, to fabricate a 75 MHz transducer element with PZT-5H, it would be approximately 25–30 μm thick or 2.5–5 grain thick, depending on the geometry used. In case of array transducers, the width of such an element, operating in bar or element mode, should be on the order of 15 μm or less to avoid an unwanted lateral resonance. Recent developments on fine grain materials have proven to be superior in dicing operations [57], and retain their bulk material properties better at higher frequencies than their larger grain counterparts [53,58].

With a breakthrough in relaxor-based ferroelectric single crystal such as lead magnesium niobate–lead titanate (PMN–PT) and lead zinc niobate–lead titanate (PZN–PT) developed since 1981, the single crystals show promising potentials to be used in high frequency transducer applications because of their superior piezoelectric properties. In comparison with polycrystalline ceramics, single crystals exhibit very high electromechanical coupling coefficients k_{33} ~ 0.85–0.95, dielectric constants ranging from 1000 to 5000 with low dielectric loss <1%, and exceptional piezoelectric coefficient d_{33} > 2000 pC/N [59,60]. High frequency (30–60 MHz) transducers fabricated from PMN–PT and PZN–PT single crystals with two-way bandwidths of 40–60% and insertion loss as high as −8 dB have been reported [61–64]. However, these single crystals have low Curie temperature T_c < 160 °C, which may limit their thermal stability during device fabrication and operation in medical imaging devices. Thus, there is currently an interest in exploring materials with similar piezoelectric properties but higher Curie temperature. It has been reported that single crystal $Pb(Yb_{1/2}Nb_{1/2})O_3–PbTiO_3$ (PYbN–PT) can achieve a Curie temperature and d_{33} as high as 360 °C and 2500 pC/N, respectively [65,66].

Because of the outstanding properties of lead-based ceramics, especially the PZT, it has been used as the material of choice for electromechanical devices, such as actuators, sensors and transducers for several decades. However, the increasing success of PZT releases more and more Pb into the environment. Due to the high toxicity of lead, the European Union (EU) included PZT in its legislature to be substituted as hazardous substances by safer materials in 2003. This directive induced a new surge in developing lead-free piezoelectric ceramics and single crystals with properties comparable to the lead-based counter. Lead-free piezoceramics with peroskite structure, such as bismuth sodium titanate $(Bi_{0.5}Na_{0.5})TiO_3$ (BNT)-based and $(K_{0.5}Na_{0.5})TiO_3$ (KNN)-based materials, exhibit high electromechanical properties. Recent reports on KNN materials modified by Li, Ta and Sb indicate that the

piezoelectric constants are comparable to those of PZT at room temperature. Table 2 shows the material properties of some BNT- and KNN-based lead free ceramics.

Single crystal lithium niobate ($LiNbO_3$) and potassium niobate ($KNbO_3$) are lead free materials that exhibit a comparable k_t to PZT, a low dielectric permittivity ($\varepsilon_{33}^{T}/\varepsilon_o \sim 35-45$), and high longitudinal sound speed ($\upsilon_L \sim 7400$ m/s), making them ideal for the design of sensitive large aperture high frequency single element transducers. Numerous transducers operating the 10–100 MHz range have been constructed using both materials [32,67,68]. The performance of these devices varied due to design differences with −6 dB bandwidths up to 75% and insertion loss values as low as −10 dB.

4.3. Piezoelectric thick film technology

To date, one of the technical challenges for fabrication of very high frequency (100 MHz–1 GHz) transducer is the processing of piezoelectric elements with a thickness in the range of 1–30 μm. Conventional thin film technologies such as sol–gel, pulsed-laser deposition (PLD), sputtering, and metal organic chemical vapor deposition (MOCVD) are not suitable to produce high quality film in this thickness range due to the slow deposition rate and high level of stress generated during the processing. On the contrary, bulk ceramic processing with sintering, lapping, dicing and bonding is time consuming and costly. Recently, piezoelectric thick film technologies that utilize modified sol–gel, aerosol and hydrothermal deposition have been reported to produce high quality thick films for device applications. The modified sol–gel process has been developed to increase film thickness by combing conventional sol–gel with ceramic powder processing which produces thick films at a relatively low temperature of about 700 °C. The aerosol deposition (AD) is a gas deposition technique for making dense, crack-free film at room temperature with a high deposition rate (up to 50 μm/min). The hydrothermal method is able to make crystalline films at low temperatures on large area substrates with different shapes in water under high pressure. Thick film technology allows one to simplify the transducer fabrication process and very high frequency transducers to be produced in a repeatable manner. The fabrication details and properties of the films derived by these three methods will be discussed in following sections. Some device examples making use of the thick film technologies will be given in Section 5.

4.3.1. Modified sol–gel method—The sol–gel method has attracted considerable interest because it has many advantages as compared to the other existing coating methods. First of all, it offers good control of film stoichiometry and chemical homogeneity. Secondly, it can produce uniform film over a large area by spin-coating technique, thus it is easy to integrate with semiconductor silicon technology for fabrications of MEMS devices, such as microsensors and microactuators. Thirdly, the production process is simple and of low-cost. The basic concept of the sol–gel method is to form a precursor solution of the elements of the desired compound in an organic solvent, to polymerize the solution into a gel, to dry and fire the gel for displacing the organic components and forming a final inorganic oxide.

Since 1980s, a number of investigators have successfully fabricated PZT film using sol–gel method with different chemical precursors. Budd et al. [80] used lead acetate, zirconium isopropoxide and titanium isopropoxide to prepare the PZT precursor solution. A single layer PZT film with thickness of 0.1 μm was prepared on Si substrate. To increase film thickness to 1 μm, multiple-spinning process was used. After the deposition of each PZT layer, the sample was pre-fired to about 300 °C. Finally, the film was sintered at a higher temperature. Yi et al. [81] used acetic acid as the solvent to prepare the precursor solution. The acetic acid could stabilize the zirconium propoxide and titanium isopropoxide to slow

NIH-PA Author Manuscript NIH-PA Author Manuscript NIH-PA Author Manuscript

down the gelation process. Ethylene glycol was also used as an additive to prevent cracking and improve the surface smoothness of the films; the thickness of film obtained this way without cracking was <2 μm. Tu et al. [82] used propanediol to prepare the PZT precursor solution and a 1 μm-thick single-layered PZT film was obtained. However, it is difficult to produce films thicker than 1 μm using conventional sol–gel methods as mentioned above.

In the view of the thickness limitation of the conventional sol–gel method, a modified sol–gel method which is also known as composite sol–gel method has been proposed [83–85]. This method involves fabrication of a composite film by depositing a layer of slurry, prepared by dispersing appropriate amount of fine ceramic powders into the sol–gel precursor solution, on a substrate followed by optimized pyrolysis and annealing steps. This approach enables the fabrication of controllable, crack-free PZT thick films (>10 μm) with minimized stress levels between various layers. The success of this process can be attributed to the formation of a strongly bonded network between the sol–gel and the ceramic particles along with enhanced adhesion to the substrate, minimizing the cracks in the resultant thick film. The ceramic particle size is in range of 100–300 nm. In addition, the significant amount of ceramic powder in the slurry can reduce the overall shrinkage of the film as demonstrated by Barrow et al. [86]. Although crack-free thick films can be prepared with composite sol–gel method, a considerable amount of micro-pores are observed leading to detrimental effects on the film properties. In order to reduce the porosity, several research groups have further modified this method by using different types of precursor or solvent, or by adding some chemicals into precursor solution. He et al. [84] reported that the bonding between the sol–gel matrix and the ceramic powder was stronger in acetic acid than that in 2-methoxethanol. Wang et al. [87] used PVA- and PEG-based dispersant to disperse the powder uniformly in the slurry.

Another new approach to yield high density PZT film is to use additional sintering aid, and repeat the process of sol gel infiltration and prolysis as demonstrated by Dorey and Whatmore [88]. 4.7 wt.% $0.2Cu_2O–0.8PbO_5$ sintering aid and 2 wt.% dispersant were added to the powder for aiding the densification of the film and stability of the slurry. The composite slurry was prepared using PZT solution-to-powder ratio of 2:3. A single composite layer was deposited on a Pt/Ti/Si substrate and fired at 450 °C. The composite layer was then repeatedly infiltrated with sol–gel precursor solution and fired to increase the film density. The desired film thickness was obtained by depositing further composite layers as described above. The final composite film with thickness of 10 μm was sintered at 710 °C for 30 min in rapid thermal annealer (RTA). This sintering temperature was selected because this was approximately 30 °C above the eutectic melting point of sintering aid. Three different piezoelectric powders (hard doped PZT, soft doped PZT and 85PMN–15PT) were used to prepare the composite films, and the resultant films had high densities with dielectric constant of 800, 900 and 1800, respectively. The piezoelectric properties ($d_{33,f}$ and $e_{31,f}$) of these films were also enhanced with four-step infiltration process [88]. Zhang et al. [89] introduced a modified method of vacuum filling sol–gel solution for improving the film density. The PZT solution-to-powder ratio was 1:1. The composite layer was deposited on Pt/Si substrate, followed by a two-stage prolysis sequence. The amorphous layer was then crystallized at 750 °C for 1 min in RTA. After placing a crystallized film into a vacuum chamber, a PZT sol–gel solution was dipped onto the film surface. Allowing a few minutes for infiltration, the film was taken out from the chamber and immediately put on a spin-coater to remove residual solution from the surface. The film was then dried and annealed again at 750 °C in RTA. The infiltration process was performed to each composite layer to obtain a dense and crack film (13 μm-thick) as shown in Fig. 5. Improvement of ferroelectric property in PZT composite film was also observed (see Fig. 6). The film with sol-gel infiltration had a remnant polarization of 16 $\mu C/cm^2$.

NIH-PA Author Manuscript NIH-PA Author Manuscript NIH-PA Author Manuscript

NIH-PA Author Manuscript

NIH-PA Author Manuscript

NIH-PA Author Manuscript

The functional properties of PZT derived by composite sol–gel also depend strongly on the mass ratio of PZT sol–gel solution-to-PZT powder in the composite solution. Wu et al. [90] have investigated the effect of solution-to-powder mass ratio on the piezoelectric and dielectric properties of the composite sol–gel films. Composite solutions with 0.3 M PZT solution-to-PZT powder mass ratios of 0.5, 1, 2, 4 and 6 were prepared. With larger solution-to-powder mass ratio, higher dielectric constant and remnant polarization was obtained as presented in Fig. 7. A linear relationship between film densities and the square root of the film dielectric constants was observed, as predicted by Nelson (Fig. 8). At a mass ratio of 6, the film density was 6700 kg/m^3, which was about 90% of bulk PZT (7500 kg/m^3). The optimized piezoelectric coefficient $e_{31,f}$ was found to be −5.8 C/m^2 when the solution-to-powder mass ratio increased to 4 (Fig. 9). Zhu et al. [91] reported that PMN–PT composite film, prepared with the solution-to-powder mass ratio of 4, exhibited good dielectric and ferroelectric property. Table 3 shows the material properties of different piezoelectric thick films derived by composite sol–gel technique.

4.3.2. Aerosol deposition method—The aerosol deposition (AD) method is a unique film formation technology that enables dense 1–100 μm thick ceramic layer (>95% of theoretical density) to be formed at room temperature by ejecting an aerosol consisting of a mixture of fine ceramic particles and gas from a nozzle placed above a substrate. This method was originally invented by Akedo and co-workers [92–95]. High deposition rate (i.e. over 30 μm/min for deposition of PZT film with area of 5 mm × 5 mm), low process temperature as well as micropatterning of PZT during deposition (without etching) [96] are very attractive for MEMS and μ-TAS (micro-total analysis system) applications [93,97,98].

The ceramic fine particle used for AD process can be prepared by either sol–gel method or mixed oxide method. The calcined ceramic powders have to be ball milled to obtain microsize of ~2 μm in diameter for AD process. As shown in Fig. 10, the ceramic powders are mixed with a carrier gas to form a colloid aerosol flow which is accelerated by the high pressure difference between the aerosol and deposition chamber, and ejected through the nozzle. The accelerated ceramic particles collide on the substrate at high speed and form a dense ceramic film at room temperature. The film deposited by AD method consisted of nanosized crystallites and an amorphous phase, thus a post-annealing process is required to improve the electrical properties by prompting grain growth and film crystallinity [99,100]. Hahn et al. reported [100] the effects of Zr/Ti ratio and post-annealing temperature on the electrical properties of 10 μm-thick PZT films fabricated by AD method. The PZT film near the MPB (52/48) showed the best overall combination of electrical properties as presented in Table 4.

Another feature of AD film is the generation of high compressive stress in the film during the deposition due to high energy impact of particles onto the substrate. This phenomenon is similar to that of sputtered film in which compressive stress is induced by the bombardment of energetic particles. In general, the residual stress can be classified into two types: intrinsic and extrinsic stresses. The intrinsic stress is related to the growth process, so it is also known as growth stress. The extrinsic stress is originated from environmental factors. One example is the thermal stress induced by the difference in the thermal expansion coefficients of the film and substrate. The residual compressive stress in the AD film is an intrinsic stress. The total intrinsic stress stored in the film increases with increasing the film thickness. Park and his co-workers [101] had demonstrated the delamination of the PZT-based films with thickness above 20 μm by AD and subsequent post-annealing process. Introduction of fine pores within the film was proposed for relieving the intrinsic residual stress. By using an organic species containing ceramic powders as the starting material, annealed AD film has a fine-grained microstructure with nano-sized pores. PZT films with thickness ranged from 20 to 100 μm showed good electrical properties [102].

NIH-PA Author Manuscript NIH-PA Author Manuscript NIH-PA Author Manuscript

Dense lead-free piezoelectric thick films of KNN were also successfully fabricated by the AD method [103]. However, the electrical properties were not good enough for practical applications. To enhance the performance of KNN film, the key approach is to shift the ferroelectric tetragonal–ferroelectric orthorhombic phase transition to lower temperature by doping, i.e. addition of lithium antimonite (LSO; $LiSbO_3$) for partial substitutions of A site ions $(Na_{0.5}K_{0.5})^+$ with Li^+, and B-site ion Nb^{5+} with Sb^{5+}. Lin et al. [104] has established a phase diagram of $(1 - x)$ KNN–xLSO system. It is well known that the morphotropic phase boundary (MPB) plays an important role in the improvement of piezoelectric properties of pervoskite lead-based piezoelectric ceramics, such as PZT and PMN–PT. MPB compositions, for example PZT with PT content close to 0.48, have anomalously high dielectric and piezoelectric properties as a result of enhanced polarizability, arising from the coupling between two equivalent energy states, that is, the tetragonal and rhombohedral phases. This allows optimum domain reorientation during poling process. Similar to lead-based system with MPB, the addition of LSO shifts the ferroelectric tetragonal-to-ferroelectric orthorhombic phase transition (T_{O-F}) close to room temperature. Coexistence of the orthorhombic and tetragonal phases can be developed at $0.05 < x < 0.07$, leading to the significant enhancement of the piezoelectric properties. As the content of LSO increases up to 0.07, a secondary phase of $K_3Li_2Nb_5O_{15}$ is formed. A KNN–LSO thick film with LSO content of 0.052 has been formed on the plantinized silicon substrate by AD process with a deposition rate of 5 μm/min [105,106]. The film was highly dense and no microcracks as shown in Fig. 11. By optimizing the post-annealing temperatures, the maximum dielectric, ferroelectric and piezoelectric properties of the KNN–LSO AD film were obtained. Table 4 lists the material properties of piezoelectric lead-based and lead-free thick films derived by AD method. These particular values were sufficiently high as to be comparable to bulk ceramics, confirming the potential use of AD films in actuators and high frequency transducer applications.

4.3.3. Hydrothermal method—Hydrothermal method is one of the low temperature synthesis techniques for fabricating piezoelectric single crystals or polycrystalline films [108–110] which depends on the solubility of raw materials in hot solvent under high pressure. The advantages of the hydrothermal method over other types of crystal growth include the ability to create crystalline phases which are not stable at the melting point and growth of large-size high quality crystals on the substrate while maintaining good control over their composition. Moreover, since raw materials react at high pressure in the hydrothermal process, high annealing temperature is not needed in this process. During the process, an autoclave is used as container of the crystallization vessels (see Fig. 12). These are usually thick-walled steel cylinders with a hermetic seal which must withstand high temperatures and pressures for prolonged period of time. Furthermore, the autoclave material must be inert with solvent. In most cases steel-corroding solutions are used in hydrothermal experiments to prevent corrosion of the internal cavity of the autoclave. Recently, Ishikawa et al. have reported PZT thick films deposited on a Ti substrate by hydrothermal method [111,112]. Starting raw materials for the reaction were lead nitrate ($Pb(NO_3)_2$ 99.0%), zirconium chloride oxide octahydrate ($ZrOCl_2{\cdot}8H_2O$ 99.0%), titanium oxide powder (TiO_2 99.0%) in potassium hydroxide (KOH) solution and titanium metal plate as the substrate. The composition of the starting material was determined as follows: 140 ml of 1 M aqueous $Pb(NO_3)_2$, 90ml of 1 M aqueous $ZrOCl_2{\cdot}8H_2O$, 1 g TiO_2, and 300 ml of 4 M KOH solution. The Ti substrates were fixed on stirrer plates made of Teflon, and the stirrers were kept in the solution. First, PZT nuclei were deposited on the Ti substrate from a solution of starting materials, and then the crystals were grown to the target thickness (10–20 μm) from the solution of starting materials. The chemical reaction of nuclear and crystal growth was processed in hydrothermal environment using an autoclave. In this process, the temperature and the pressure inside of autoclave were 160 °C and 0.55 MPa,

respectively. The reaction time was about 12 h for each process. The fabricated hydrothermal PZT thick film was about 20 μm thick after 10 times deposition process. However, based on the SEM observation, hydrothermal PZT films had some holes among the grains.

In order to increase the density of films and allow self-separation of the deposited hydrothermal film from the substrate, Zhu et al. [113] proposed to use sol–gel vacuum filling technology followed by high temperature annealing process. The hydrothermal PZT thick films with Ti substrate were annealed at a suitable temperature for 2 min by RTA (rapid thermal annealing) in atmosphere. Then, the PZT thick films (sample A) could separate from the Ti substrate itself without any crack. Some self-separation films (sample B) were sintered at 950 °C for 1 h in furnace. Some self-separation films (sample C) were firstly immersed in PZT solution prepared by the vacuum filling method for 10 min, after 2 min heat treatment on hot plate at 200 °C and 400 °C and 1 min rapid thermal annealing at 650 °C, these films were sintered at 950 °C for 1 h in furnace.

The XRD pattern of hydrothermal PZT thick films on Ti substrate before thermal treatment is shown in Fig. 13. Results showed that the films appeared to be well crystallized and had the pure perovskite phase without any observable second phase, indicating that PZT thick films fabricated by hydrothermal method were randomly oriented and in polycrystalline structure using Ti as substrate.

Fig. 14 shows the SEM surface pictures of the self-separation hydrothermal PZT thick films with different conditions. Though sample A is the roughest one, it is crack-free, indicating that thermal stress relaxation is not through crack formation. The surface of sample B becomes smooth because high temperature sintering makes grains grow more uniformly. Sample C has the smoothest surface because PZT solution infiltration into the pores and makes the film much denser than sample A.

The dielectric constants and dielectric losses of sample A, B and C vary slightly with frequencies from 1 kHz to 1 MHz (Fig. 15). It can be seen that no matter what frequency it is, the dielectric constant of sample C is always larger than those of samples A and B. At 1 kHz, the dielectric constants of samples A, B and C are 374, 465 and 593, respectively. From 1 kHz to 1 MHz, the dielectric losses of samples B and C are similar and little lager than that of sample A, but are still in the range of 0.033–0.05, which is low enough for device applications.

The ferroelectric hysteresis loops of three types of PZT thick films are shown in Fig. 16. The hysteresis loops of samples B and C exhibit good symmetry, but sample A has an asymmetry loop. It can be seen that the remnant polarizations P_r of samples A, B and C are 8.4, 20.9 and 30.5 μC/cm^2, respectively. The P_r of sample C is close to that of PZT bulk materials sintered at high temperature, which is 35 μC/cm^2. Sample A is the easiest one to be broken down under application of high electric field due to presence of pores. The results suggest that high temperature sintering and solution filling can enhance the dielectric and ferroelectric properties of self-separation hydrothermal PZT thick films.

5. Piezoelectric high frequency films devices

5.1. Sputtered ZnO film transducer by MEMS process

Zinc oxide (ZnO) has one of the defining characteristics of a piezoelectric material which is the lack of a center of symmetry in the unit cell. Fig. 17 shows the crystal structure of ZnO [114]. ZnO is a wurzite material and is non-ferroelectric with small dielectric constant (about 10). It shows a piezoelectric response along [0 0 1] direction. Acceptable

NIH-PA Author Manuscript NIH-PA Author Manuscript NIH-PA Author Manuscript

NIH-PA Author Manuscript
NIH-PA Author Manuscript
NIH-PA Author Manuscript

piezoelectric effect, greater stability and availability make it being one of the most popular piezoelectric materials for thin-film device applications. In addition to piezoelectric devices, ZnO is used in a variety of other scientific applications including acoustic wave devices, photoconductors, and optical waveguides and nanowire devices [115,116]. Therefore, many different deposition methods have been developed such as sol–gel process [117], spray pyrolysis [118], molecular beam epitaxy (MBE) [119] and sputtering [120–122]. Sputtering is the most commonly used deposition method for ZnO films because it is possible to grow oriented thin films with uniform thickness on a wide variety of substrates. A novel fabrication process of high frequency transducers based on sputtered ZnO film was introduced as follows.

At high frequencies, acoustic attenuation in a medium may become very significant, so the focal point of the transducer must be located very close to the transducer surface. The rationales for employing strongly focused, high frequency transducers are twofold: to obtain higher intensity at the focus, and to achieve superior lateral resolution. Since the addition of a lens will generate additional attenuation, self-focused transducer is preferred in high frequency transducer fabrication process.

Up to now, several investigators have reported using laser machining to obtain spherical surfaces on sapphire to create focused acoustic beams [115], while others have tried to make spherical surfaces from flat planar PVDF film by vacuum sucking [123]. Recently, MEMS technology has shown great promise for device fabrication [124]. Photolithography, along with thin film deposition and etching technology, allows a large amount of batch-processed devices to be produced at one time at a low-cost with reliable performance. Conventional photolithography is very effective at making planar devices, but has several drawbacks in making a curved device with this technology.

The axial and lateral resolutions of a transducer are determined by the emitted pulse duration and the beam width of the transducer, respectively. The beam width at the focal point of a transducer, W_b, is linearly proportional to the wavelength by the relationship: $W_b \approx \lambda F\#$, where $F\#$ is the *f*-number defined as the ratio of the focal distance to the aperture dimension, and λ the wavelength. The depth of focus D_f, defined as the region where the intensity of the beam is maximal, is also linearly related to the wavelength by the relation: $D_f = 7.1\lambda(F\#)^2$. Thus, from these relationships, it is clear that an increase in frequency and a decrease of wavelength can improve both lateral and axial resolutions. Another way to obtain better lateral resolution at a certain axial distance is to take advantage of acoustic focusing. Modified MEMS fabrication technique can be used to design focused, dome-shaped-diaphragm transducers with a readily adjustable *f*-number [125]. Fig. 18 illustrates the design of a focus transducer. The dimension *d*, which is the aperture size, is determined by silicon bulk-micromachining. The transducer focal region (*a*, *b*, *c*) can be determined by the diameters of the ball that is chosen.

The precisely sized spherical balls with surface roughness less than 0.2 μm from Bal-Tec, Inc. was used to fabricate a piezoelectric Micromachined Ultrasonic Transducer (pMUT)-based on dome-shaped-diaphragm transducer (DSDT). A 3-inch silicon wafer was used as a substrate for the demonstration of the fabrication idea. The dome-shaped parylene diaphragms (6–10 μm thick) was developed by low temperature wax molding process. This greatly reduced the thermally induced stress of the polymer material so that the resultant geometry of the 3D parylene diaphragm conformed to the contour of the chosen spherical ball [126]. Based on PiezoCAD modeling for ZnO transducer, the lateral dimension of the pMUT-DSDT was chosen to be 2.5 mm so that the electrical impedance of the transducer at 200 MHz was matched to that of the electrical power source (~50 Ω). This dimension was larger than that of a PZT transducer, since the dielectric constant of ZnO was about 150

NIH-PA Author Manuscript NIH-PA Author Manuscript NIH-PA Author Manuscript

times less than that of PZT. Thus, in order to match the electrical impedance, relatively large lateral dimension for the diaphragm was used. Fig. 19 shows the fabrication process of the pMUT-DSDT. First, 0.3 μm thick silicon nitride was deposited on the silicon wafer using LPCVD. This process was followed by photolithography and reactive ion etching to remove some of the silicon nitride to make square openings at the designated locations. Then KOH (44%) solution was heated up to 80 °C for wet etching to obtain through holes on the processed wafer. After choosing appropriately sized spherical balls and spreading them onto the processed wafer, the balls were then fit to each of the square thru holes. Once the balls were fitted into all the square openings on the wafer, the wafer edge was secured to a holder with vertical position adjustment. A wax mold was formed by taking out the balls after the wax was cooled down and solidified. Fig. 20 shows the resultant wax mold on the silicon substrate. Next, 8 μm thick parylene was conformally deposited on the processed wafer. The wax mold was removed by toluene solvent at room temperature, which avoided thermally induced stress in the parylene at elevated temperature. As a result, the spherically shaped diaphragms were produced on the silicon wafer substrate as shown in Fig. 21.

The active material of the pMUT-DSDT uses sputtered ZnO film, which makes its *C*-axis oriented perpendicularly to the dome surface. To overcome the shortcoming of planar photolithography, shadow masks have been used to selectively deposit the bottom aluminum electrode, ZnO layer, and top aluminum electrode. One key idea of the fabrication process is to use the 0.5 μm-thick aluminum electrodes also as a supporting structural layer. Since the ZnO is deposited at 250 °C, the temperature will alter the shape of parylene diaphragm, due to the thermally induced stress in the parylene, if there is no other structurally rigid material in the diaphragm. However, once the parylene is coated with A174 promoter, which provides good adhesion to the deposited aluminum, the subsequent ZnO sputtering process does not affect the designated spherical shape, since the aluminum provides enough structural stiffness. At the 200 MHz designated frequency, the half-wavelength thickness of ZnO film (for a longitudinal acoustic resonance in the thickness direction) is approximately 13 μm. Fig. 22 shows the SEM photograph of its cross section. The crystalline quality of the films was examined by XRD and the results are shown in Fig. 23. The XRD patterns of 1-μm-thick ZnO films consist of three peaks which are indexed as ZnO (0 0 2), Si substrate and Al (1 1 1) electrode respectively. It can be seen that sputtered films exhibit only the ZnO (0 0 2) peak since ZnO films grow with strong $\langle 0\ 0\ 1 \rangle$ preferred orientation due to its lowest surface free energy [127].

To make a functional pMUT-DSDT, suitable backing and matching layers are also needed. The best backing material should have an acoustic impedance similar to that of the transducer and absorbs the energy that enters it as much as possible when no matching layers are used. Thus, the low impedance parylene supporting layer (~3 MRayl) is not a good choice for a backing material. The spherical cavities of the processed pMUT-DSDT devices are first filled with low melting temperature wax (60 °C) and mounted to a glass plate (Step 8 in Fig. 19). To remove the parylene layer, we used oxygen reactive ion etching at 100Wand 100 mtorr for 25 min. After the parylene support layer is removed, the transducer membrane is mainly composed of 13.5 μm thick ZnO film whose acoustic impedance is 36 MRayl. Then a hollow alumina pillar is glued to the back of each DSDT as the transducer housing to contain the silver epoxy. A conductive epoxy, E-Solder (vonRoll Isola), is applied directly to the back surface and held in place by the alumina housing. It is then centrifuged for 10 min at 2000 rpm to remove air and maximize acoustic impedance. After curing, the DSDT is removed from the glass plate by heating the wax and removing the wax with acetone. To further improve the performance of the pMUT-DSDT, a 3 μm-thick parylene was deposited on the front-face of transducer as the matching layer. Finally, individual pMUT-DSDTs are diced from the whole wafer.

NIH-PA Author Manuscript NIH-PA Author Manuscript NIH-PA Author Manuscript

To estimate the performance of the transducer with the model's predictions [128], the electrical impedance characteristics of the transducer are shown in Fig. 24. The resonant frequency is approximately 215 MHz, with a corresponding impedance of about 14 Ω. The phase has a peak at about −20° and a phase change of about 5°. The electromechanical coupling coefficient k_t in the single crystal can be determined from [129]

$$k_t=\sqrt{\frac{\pi}{2}\frac{f_r}{f_a}\tan\left(\frac{\pi}{2}\frac{f_a-f_r}{f_a}\right)} \quad (5.1)$$

where f_r is the resonant frequency and f_a is the antiresonant frequency. According to Eq. (5.1), $k_{t,eff}$ is about 0.28 which is within the generally accepted range of 0.24–0.29 for ZnO [130].

Impedance analysis is followed by pulse-echo testing with a Panametrics 400 MHz receiver and pulser/preamplifier [131]. The testing is performed in water at 25 °C using a quartz target as the reflector. In pulse-echo mode, the pulser is used to generate a broadband electrical pulse signal and is connected by a coaxial cable to the transducer. The piezoelectric element responds to the pulse by emitting an ultrasonic wave at its resonant frequency. The reflected ultrasonic wave is received by the transducer, and the electrical signal induced in the piezoelectric element is sent via coaxial cable to the receiver. The receiver then amplifies and filters the signal and sends its output to a 1 GHz LeCroy digital oscilloscope to be viewed and recorded. The oscilloscope is also used to take the FFT of the received echo to determine the transducer center frequency and bandwidth. Fig. 25a shows the echo waveform received from the target during pulse-echo testing. Fig. 25b is the frequency spectrum of that waveform. The bandwidth at −6 dB was found to be 28% centered at 200 MHz, which is close to the model's predictions.

For this high frequency device, the electrical impedance is lower than 50 Ω. Increasing the impedance matching to 50 Ω could be accomplished by decreasing the aperture size which may decrease the sensitivity. Another change to be considered is the use of two matching layers to improve the transducer bandwidth and sensitivity. The development of nano-composite matching layer with a wide range of acoustic impedances is needed for high frequency transducer [132]. The device exhibits a noticeable ringdown due to the 36 MRayl ZnO thin film against the relatively low acoustic impedance E-solder backing.

5.2. Single element thick films transducers

To simplify the transducer fabrication process and allow very high frequency transducers to be produced in a precisely controlled, repeatable manner, the piezoelectric thick film technology is one of the best choices. Lukacs et al. [133] demonstrated that single element high frequency transducers could be fabricated with a composite sol–gel PZT film. The center frequency of the transducer is in range of 70–160 MHz, with −6 dB bandwidth of 16–52%. In this case, Al was used as the substrate for PZT thick film deposition, and then etched it off simply with a NaOH solution to form a silver epoxy backed transducer. However, the Al substrate limits the sintering temperature for PZT film (below 600 °C). It is known that the properties of PZT film can be improved by increasing the sintering temperature. To produce high quality PZT thick film, plantinized Si substrate has been used for high temperature sintering. Buffer layers with a sequence of Pt/Ti/SiO_2/Si can be used to prevent interfusion and oxidation reactions of piezoelectric layer with silicon while Ti is used as an adhesion layer. High performance PZT and PMN–PT composite thick films have been successfully formed on the plantinized Si substrate with aid of vacuum filtration during

deposition process and high sintering temperature. The deposited films exhibit better dielectric and ferroelectric properties for high frequency transducer applications (see Table 5).

Although Si has a large acoustic impedance (17 MRayl), it is not suitable as a backing layer of the transducer due its low acoustic attenuation. An acoustically lossy and electrically conductive epoxy, E-solder 3022 (supplied by Von Roll Isola Inc.), has been used as backing. As shown in Fig. 26, both conventional technology and silicon etching technique have been involved in the transducer fabrication process. In one approach [89], E-solder was cast on the Cr/Au electrode following by removal of Si substrate with either XeF_2 dry etching or KOH wet etching. E-solder backed sample was then mounted in an SMA connector, and a 150 nm-thick Cr/Au was sputtered across the element and metal housing to form a ground electrode. A hot press focus method was used to focus the transducer. A spherical ball bearing was gently pressed into the PZT film surface at 60 °C to form a curved surface. The PZT composite film with thickness below 20 μm had a lower risk of cracking during the press-focusing process than $LiNbO_3$ single crystal or bulk PZT because it was far less brittle. When a PZT composite film with a thickness of 18 μm and diameter of 1.2 mm was used, a spherical ball with a diameter of 3 mm was chosen for pressing in order to fabricate a transducer with an *f*-number of 1.25. The transducer had a center frequency of 103 MHz and −6 dB bandwidth of 70% (Fig. 27). Using Eq. (1.1): $R_{\text{axial}} = c_{\text{water}}/(2 f_c BW)$ [134], a 9.2-μm axial resolution was expected for this transducer by calculation.

A 8-μm diameter tungsten wire was used as the target and mounted to the three-axis positioning system for a two-way lateral beam profile test. Both the transducer and the wire were placed in a water tank filled with distilled water. Using the same setup for the pulse-echo measurement, the receive signals obtained from scanning the wires were displayed on a digital oscilloscope which was connected to the computer via an IEEE-488 interface. The transducer had a lateral resolution of 33 μm at −6 dB. Efforts have been made to fabricate high frequency transducers with different piezoelectric elements. As shown in Table 5, 100–200 MHz transducer with −6 dB bandwidth of 50–70% were obtained by using the piezoelectric thick film derived by composite sol–gel method and aerosol deposition.

5.3. PZT composite linear arrays

5.3.1. Kerfless linear array—Fabrication of high frequency (30–50 MHz) ultrasonic linear arrays is still a challenge. The task is even more difficult to build arrays at a frequency higher than 100 MHz, which has the potential to provide more detailed skin texture for early diagnosis of melanoma or to image small objects as stem cells. Recent research shows that the microfabrication approach can be used to produce such high frequency arrays [10,11,136–138]. PZT thick film derived by composite sol–gel method has been shown to exhibit acceptable dielectric and piezoelectric properties making it a good candidate for fabricating high frequency ultrasonic transducers as presented in previous section.

Wu et al. [139] reported a very high frequency (beyond 100 MHz) kerfless linear array with 12 μm-thick PZT composite sol–gel film by using micro-machining process. A mask for patterning the 32-element linear array had a kerf of 12 μm (Fig. 28), an element width of 24 μm and an element length of 4 mm. The fabrication process is illustrated in Fig. 29. An insulating layer of 1-μm Si_3N_4 was deposited on PZT thick film and patterned to leave an opening for the working area of the linear arrays. A layer of Au/Cr was deposited on the top surface and pattered as the top electrodes by photolithography. Based on our previous experience, thick Au/Cr electrode will damp the center frequency. Thus, the thickness of Au/Cr is optimized as 1000 Å/500 Å which only damp −1 MHz of center frequency. The backside silicon under the working area was etched with a XeF_2 drying etching. Subsequently, the layer of SiO_2 was removed by BOE. Finally, a conductive epoxy (E-

NIH-PA Author Manuscript NIH-PA Author Manuscript NIH-PA Author Manuscript

Solder 3022) was used as a backing material, and at the same time, provided the electric connection for the backside electrode. Fig. 30 shows the photos of the device fabricated. The pulse-echo response of PZT composite array is presented in Fig. 31. The composite array transducer has a center frequency of 120 MHz, and −6 dB bandwidth of 45%. To further improve the bandwidth of the array, a layer of 5 μm-thick parylene was deposited on the front surface of the arrays as the matching material, and the −6 dB bandwidth was increased to 60%. The measured insertion loss is found to be ~−40 dB. For comparison, a commercial PZT-5H sheet was used to build a linear array with similar structure and fabrication process. The PZT-5H array has a center frequency of 128 MHz, −6 dB bandwidth of 40% and insertion loss of −28 dB. The experimental results suggest that PZT composite array may be useful in broad bandwidth application because its relatively low acoustic impedance (15–20 MRayl) compared with PZT-5H materials (~30 MRayl). The PZT-5H array has better sensitivity because of its higher coupling coefficient ($k_t = 0.55$) than that of PZT composite film ($k_t = 0.34$).

5.3.2. Micro-machined linear array—Lower-frequency (2–30 MHz) arrays typically use mechanical dicing to separate array elements, whereby elements are cut from a plate of piezoelectric ceramic or single crystal and back filled with a polymer filler [140]. This technique generally has been limited to arrays designed to operate in less than 20 MHz range. However, in recent years, several studies have proven that it is viable option for manufacturing arrays with operational center frequencies up to 30 MHz [141–143]. The most sophisticated of the arrays built was the 128-element 30 MHz 1–3 piezo-composite array developed by Michau et al. [143]. Alternatively, a 48-element 30 MHz array was developed using a patented process of bonding thin plates of piezoceramic with a carefully engineered microsphere-loaded polymer to create a 2–2 piezocomposite matrix [144], which was then mechanically diced to form individual array element [145]. More recently, Cannata et al. [146] have pushed the high frequency piezocomposite array to 35 MHz using a precise dicing method. However, the assembly of such transducer array with bulk ceramics can be difficult because of limitations brought about by the cutting and shaping of the thin piezoceramics. A micro fabrication process based on MEMS technology may be one the of methods to solve these problems in fabricating high frequency ultrasound array with thick films although the kerfless approach is a simpler option as described in previous section. The increased crosstalk between adjacent elements is always an inevitable issue in kerfless array.

One of the effective ways to reduce the crosstalk is the mechanical isolation between elements. Laser dicing is an option for producing high-frequency array (>50 MHz), but the cost may be prohibitive. Deep reactive ion etching (DRIE) has been widely used in etching PZT thin films for ferroelectric memory application [147]. Recently, new advances in PZT dry etching have been reported [148–150]. Pure sulfur hexafluoride (SF_6) or a mixture of SF_6 and Argon (Ar) were used as etching gases in plasma etching of PZT film. The advantages of fluorine chemistry are its good selectivity to mask materials and its relatively high etching rate, which can reach values as high as 0.25 μm/min. Since the components produced by the etching process have significantly higher boiling temperatures, their removal is inefficient. In closely spaced structures, this would result in sidewall angles less than 80°, which is unacceptable for fabricating high frequency arrays. Recently, Marks et al. [151] reported that the use of chlorine-based etching gases with an elevated wafer temperature yielded good vertical etch profiles and a higher etching rate. The dry etching mechanism of PZT in chlorinated gas plasmas has been investigated in detail [152,153], and several measures have been proposed to minimize etching damage to the PZT material during the process [154].

NIH-PA Author Manuscript NIH-PA Author Manuscript NIH-PA Author Manuscript

NIH-PA Author Manuscript

NIH-PA Author Manuscript

NIH-PA Author Manuscript

Zhou et al. [155] reported the design, fabrication and characterization of a 32-element high-frequency linear array (with center frequency up to 80 MHz) using DRIE dry etching technique with high quality PZT composite sol-gel thick films. In this design, the linear array has the kerf of 12 μm, the element width of 24 μm and element length of 4 mm. The PZFLEX program was used to predict the azimuthal beam profile for eight elements to investigate the impact of grating lobes. A transmitting grating lobe was expected near 40° (Fig. 32a). The feasibility of imaging with the array was simulated using a FieldII program. As shown in Fig. 32b, the array can be well focused at 1–1.5 mm when a phantom with five point scatter was chosen as the target. To transfer the designed array pattern onto PZT film surface, a 4 μm-thick Ni hard mask was formed by electroplating process and patterned by photolithographic method. The area underneath the Ni hard mask was protected and the rest of area was etched off by chlorine gas plasma. The etching parameters have been optimized with ICP power of 600 W, dc bias voltage of 200 V, 20 sccm of Ar and 60 sccm of Cl_2. The etching rate of PZT film was 8 μm/h and the sidewall angle of the elements >85°(Fig. 33a). The kerfs were infiltrated with epoxy (Fig. 33b). The backside silicon under the working area was etched with XeF_2 and followed by conductive epoxy filling. The prototype array was housed in a copper tube. The poling process was carried out after deposition of the top electrode. A layer of parlyene was deposited to serve as a matching. The array has the center frequency of ~80 MHz and −6 dB bandwidth of 60% (Fig. 34). A crosstalk of around −31 dB was measured between 50 MHz and 90 MHz. The insertion loss of −41 dB was obtained at the center frequency. The relatively high insertion loss is mainly due to small coupling coefficient of the PZT composite film ($k_t = 0.34$). There is still a large space to further improve the functional properties of PZT film, making it comparable to bulk PZT materials.

6. Current problems and future directions

The field of medical ultrasound imaging is progressing rapidly. As its resolution and cost-effectiveness compares favorably with X-ray computed tomography and magnetic resonance imaging, the market share of ultrasound imaging is expected to gradually increase. High frequency ultrasound has many clinical applications including visualizing blood vessel wall, anterior segments of eye and skin. Another application of the high frequency transducer is small animal imaging. It is especially attractive in imaging the heart of small animals like mouse which has a size in the mm range and a heart rate faster then 600 BPM. However, mechanical scanning of a single element transducer for imaging has two main drawbacks: poorer resolution and motion of probe. Single element transducers can only produce beams with a fixed focus which means the spatial resolution of the device is best only within the depth of focus, i.e. in a very tight zone and degrades rapidly beyond the focal point. Mechanical motion of the transducer limits the frame rate and may cause patient discomfort, and, at worst, may be hazardous to the patient. These problems can be overcome by adopting linear arrays which use electronic scanning to form an image slice and therefore can achieve higher image frame rates. In Section 5, the current development of high frequency single element transducers at frequency as high as 200 MHz and arrays at 80–120 MHz were presented.

Efforts have to be made to further improve the performance and increase the frequency of these devices. As reported, the electromechanical coupling coefficient of the PZT film ($k_t \sim 0.34$) is lower than that of the bulk sample ($k_t \sim 0.55$), resulting in lower sensitivity. Besides, high crosstalk is observed in high frequency arrays due to their small size. To suppress crosstalk, one can use better kerf filler e.g. an epoxy containing air balloons. Moreover, there is still a challenge to enhance the functional properties of the piezoelectric material and make them comparable to bulk PZT sheet. For the composite sol–gel process, one can optimize the spin-coating procedure (such as spin-coating speeds and durations), solution vacuum-filling procedure (such as vacuum pressure, duration and filling sequence), sintering

NIH-PA Author Manuscript

NIH-PA Author Manuscript

NIH-PA Author Manuscript

temperature, poling conditions, etc. [134,139]. Doping of piezoceramic film is also an effective way to enhance the film properties [156,157]. New methodologies, such as hybrid process involving the sol–gel method and laser ablation, have been reported to produce high quality piezoelectric film for micro-device applications [158].

High frequency ultrasound may find other significant biomedical applications such as acoustic microscopy for non invasive investigation of living cells (not only to visualize the cells but also examine their mechanical properties) [159,160], and acoustic tweezers for non contact manipulation of microparticles or cells based on radiation force principle [161,162]. As the size of the biological structures varies from 1 μm to 200 μm, the transducers have to be in the frequency range between 50 MHz and 1.5 GHz to obtain the required resolution. Conventional transducer fabrication process is capable of producing a self-focus transducer with frequency close to 200 MHz only. Thus, another important challenge in high frequency transducer is the device fabrication process. More recently, a silicon based acoustic lens has been developed incorporation with thick film technology to fabricate the transducer up to GHz range [160,163]. In this approach, as shown in Fig. 35, acoustic lenses were produced by first etching the spherical cavity into one side of a silicon wafer and deposition of a piezoelectric film on the backside. The focal distance q of a high frequency transducer is a compromise between the maximal acceptable insertion loss of the transducer, the minimal allowed working distance w and the possibility to realize small radii of curvature r. Usual specifications for transducers in the GHz range are: (a) focus distance q of 50–80 μm and (b) lens aperture size $2a$ of 100–400 μm. Fig. 36 shows the REM images of an acoustic lens and a ZnO based 1-GHz transducer. To produce a GHz transducer, the piezoelectric film thickness is in range of several micrometers. Jakob et al. [163] has realized high frequency PZT film transducer with sol–gel and MOCVD technologies and compared their performance to ZnO based 1-GHz transducers. The sol–gel route PZT transducers have signal amplitude and bandwidth comparable to the ZnO transducer. The sol–gel transducers have the potential to reach higher amplitude by matching the electrical impedance from 5 Ω to 50 Ω. Integration of piezoelectric thick film technology with MEMS device processing is expected to open new possibility for very high frequency transducer and arrays in the future, and their applications can be further expanded into other biomedical disciplines.

7. Conclusions

This article reviews the recent developments in piezoelectric films for high frequency ultrasonic transducer applications. Three main thick films technologies for piezoelectric materials that have been investigated are discussed. Higher than 200 MHz piezoelectric ZnO, PZT and lead free single element transducers have been successfully fabricated. With a better spatial resolution, these transducers are useful for observing biological structure with resolution approaching 10 μm. By integration with MEMS technology, different designs of high-frequency linear arrays have also been achieved. Very high frequency (up to GHz) piezoelectric PZT transducers are also discussed. There is no reason not to believe that in the near future very high frequency piezoelectric transducers will become more widely available and their applications expanded into not only medical diagnostics but also the fields of cellular bioengineering and lab-on-chip devices.

Acknowledgments

We would like to acknowledge Dr. B.P. Zhu, Dr. C.G. Liu, Dr. F.T. Diuth, Dr. G.H. Feng, Dr. J. Cannata, Dr. C. Hu. Dr. M. Ishikawa, D.Y. Huang, Dr. J. Lee, Ms. A. Jakob, Mr. J. William, Mr. L. Xiang, Mr. R. Chen and Mr. H. Chabok. Without their significant contributions, the overview cannot be finished. Special thanks are extended to Prof. Susan Trolier-McKinstry at Penn State University, Prof. E.S. Kim at USC MEMS group, Prof. Takamuta at Toin University of Yokohama in Japan, Dr. J.H. Ryu at Korea Institute of Materials Science (KIMS), Prof. W. Ren

at Xi'an Jian Tong University in China. This work is financially supported by NIH P41-EB2182, 1R43CA110214-01 and 1R43 RR014127-01A1.

References

1. Scott JF, De Araujo CAP. Science. 2000; 246:1400–3. [PubMed: 17755995]
2. Muralt P. J Micromech Microeng. 2000; 10:136–46.
3. Bernstein JJ, Finberg SL, Houston K, Cross LE. IEEE UFFC. 1997; 44:960–7.
4. Zhang QQ, Djuth FT, Zhou QF, Hu CH, Cha JH, Shung KK. Ultrasonics. 2006; 44:711–5.
5. Kawai H. J Appl Phys. 1969; 8:975–9.
6. Zou W, Holland S, Kim KY, Sachse W. Ultrasonics. 2003; 41:157–61. [PubMed: 12726936]
7. Foster FS, Harasiewicz KA, Sherar MD. IEEE Trans Ultrason Ferroelect Freq Contr. 2000; 47:1363–71.
8. Sherar MD, Noss MB, Foster FS. Nature. 1987; 330:493–5. [PubMed: 3683563]
9. Shung KK, Cannata JM, Zhou QF. J Electroceram. 2007; 19:139–45.
10. Mina IG, Kim H, Kim I, Park SK, Choi K, Jackson TN, et al. IEEE Trans Ultrason Ferroelect Freq Contr. 2007; 54:2422–30.
11. Pang G, Sayer M, Lockwood GR, Watt M. IEEE Trans Ultrason Ferroelect Freq Contr. 2006; 53:1679–84.
12. Dauchy F, Dorey RA. J Electroceram. 2007; 19:383–6.
13. Muralt P. Integr Ferroelectr. 1997; 17:297–307.
14. Martin PM, Good MS, Johonston JW, Posakony GJ, Bond LJ, Crawford SJ. Thin Solid Films. 2000; 379:253–8.
15. Setter N, Damjanovic D, Fox G, Gevorgian S, Hong S, Kingon A, et al. J Appl Phys. 2006; 100 [051606-1].
16. Sugiyama S, Takagi A, Tsuzuki K. Jap J Appl Phys. 1991; 30:2170–6.
17. Barrow DA, Petroff TE, Sayer M. Surf Coat Technol. 1995; 76:113–7.
18. Lukacs M, Sayer M, Foster FS. IEEE Trans Ultrason Ferroelect Freq Contr. 2000; 47:148–59.
19. Dausch DE, Castellucci JB, Chou DR, Von Ramm OT. Proc IEEE Ultrason Symp. 2006:934–7.
20. Curie P, Curie J. Comptes Rendus (France). 1880; 91:294–5.
21. IEEE standard definitions of terms associated with ferroelectricrelated materials. IEEE Trans Ultrason Ferroelectectr Freq Contr. 2003; 50:1613.
22. Royer D, Kmetik V. Electron Lett. 1992; 28:1828–30.
23. Shepard JF Jr, Moses PJ, Trolier-McKinstry S. Sens Actuat. 1998; A71:122–38.
24. Shung, KK. Diagnostic ultrasound: imaging and blood flow measurements. Vol. 3. CRC Press; 2006. p. 39-77.
25. Krimholtz R, Leedom D, Matthaei G. Electron Lett. 1970; 6:398–9.
26. Kinsler, LE.; Frey, AR.; Coppens, AB.; Sanders, JV. Fundamentals of acoustics. 3. New York: John Wiley & Sons; 1982.
27. Desilets CS, Fraser JD, Kino GS. IEEE Trans Sonics Ultrason. 1978; 25:115–25.
28. Lau ST, Li H, Wong KS, Zhou QF, Zhou D, Li YC, et al. J Appl Phys. 2009; 105:094908.
29. Wang SX, Carlier J, Ndieguene, Campistron P, Debavelaere DC, Soyer C, et al. Proc IEEE Ultrason Symp. 2008:678–81.
30. Zhou QF, Cha JH, Huang Y, Zhang R, Cao W, Shung KK. IEEE Trans Ultrason Ferroelect Freq Contr. 2009; 56(1):213–9.
31. Tiefensee F, Becker Willinger C. Proc IEEE Ultrason Symp. 2009:1719–21.
32. Cannata JM, Ritter TA, Chen WH, Silverman RH, Shung KK. IEEE Trans Ultrason Ferroelect Freq Contr. 2003; 50:1548.
33. Webster RA, Button TW, Meggs C, MacLennan, Cochran S. Proc IEEE Ultrason Symp. 2007:1925–8.
34. Goldberg, RL.; Smith, SW. Transducers. In: Bronzino, J., editor. The biomedical engineering handbook. Boca Raton (FL): CRC Press; 1994. p. 1077-92.

NIH-PA Author Manuscript NIH-PA Author Manuscript NIH-PA Author Manuscript

NIH-PA Author Manuscript NIH-PA Author Manuscript NIH-PA Author Manuscript

35. Hunt JW, Arditi M, Foster FS. IEEE Trans Biomed Eng. 1983; 30(8):453–81. [PubMed: 6629380]
36. IEEE standard on piezoelectricity. ANSI/IEEE Std; 1987.
37. Kim M, Kim J, Cao WW. Appl Phys Lett. 2006; 89:162910.
38. Kim M, Kim J, Cao WW. J Appl Phys. 2006; 99:074102.
39. Kim J, Kim J, Cao WW. Appl Phys Lett. 2007; 91:152904.
40. Brown LF. IEEE Trans Ultrason Ferroelect Freq Contr. 2000; 47:1377.
41. Measurement Specialties Inc. www.meas-spec.com
42. Kino, GS. Acoustic waves: devices, imaging, and analog signal processing. New Jersey: Prentice Hall; 1987.
43. Zipparo MJ, Shung KK, Shrout TR. IEEE Trans Ultrason Ferroelect Freq Contr. 1997; 44:1038.
44. Snook KA, Hu CH, Shrout TR, Shung KK. IEEE Trans Ultrason Ferroelect Freq Contr. 2006; 53:300.
45. Zhang R, Jiang B, Cao W. J Appl Phys. 2001; 90:3471.
46. H.C. Materials Corporation. <www.hcmat.com>
47. Sherar MD, Foster FS. Ultrason Imag. 1989; 11:75.
48. Ketterling JA, Aristizábal O, Turnbull DH, Lizzi FL. IEEE Trans Ultrason Ferroelect Freq Contr. 2005; 52:672.
49. Davis GT, Broadhurst MG, Lovinger AJ, Furukawa T. Ferroelectrics. 1984; 57:73–84.
50. Koga K, Ohigashi H. J Appl Phys. 1986; 59:2142–50.
51. Goldberg RL, Smith SW. IEEE Trans Ultrason Ferroelect Freq Contr. 1994; 41:761–71.
52. Zipparo MJ, Shung KK, Shrout TR. IEEE Trans Ultrason Ferroelect Freq Contr. 1997; 44:1038–48.
53. Chan HLW, Lau ST, Kwok KW, Zhang QQ, Zhou QF, Choy CL. Sens Actuat A. 1999; A75(3): 252–6.
54. Muralt P, Ledermann N, Paborowski J, Barzegar A, Gentil S, Belgacem B, et al. IEEE Trans Ultrason Ferroelect Freq Contr. 2005; 52:2276–88.
55. Snook KA, Hu CH, Shrout TR, Shung KK. IEEE Trans Ultrason Ferroelect Freq Contr. 2006; 53(2):300–8.
56. Brown JA, Foster FS, Needles A, Cherin E, Lockwood GR. IEEE Trans Ultrason Ferroelect Freq Contr. 2007; 54(9):1888–94.
57. Hackenberger WS, Kim N, Randall CA, Cao W, Shrout TR. Proc IEEE Appl Ferroelect. 1996; 2:903.
58. Ritter TA, Shung KK, Cao W, Shrout TR. J Appl Phys. 2000; 88:394.
59. Park SE, Shrout TR. IEEE Trans Ultrason Ferroelect Freq Contr. 1997; 44:1140–7.
60. Rajan KK, Shanthi M, Chang WS, Jin J, Lim CL. Sens Actuat A. 2007; 133:110–6.
61. Zhou QF, Xu X, Gottlieb EJ, Sun L, Cannata JM, Ameri H, et al. IEEE Trans Ultrason Ferroelect Freq Contr. 1997; 44:1140–7.
62. Zhou QF, Wu DW, Jin J, Hu CH, Xu XC, Williams J, et al. IEEE Trans Ultrason Ferroelect Freq Contr. 2007; 54:668–75.
63. Peng J, Lau ST, Chao C, Dai JY, Chan HLW, Luo HS, et al. Appl Phys A: Mater Sci Process. 2010; 98:233. [published online in August 2009].
64. Lau ST, Zhou LB, Chan HLW. Sens Actuat A. 2010; 167:78–82.
65. Zhang S, Priya S, Furman E, Shrout T, Randall C. J Appl Phys. 2002; 91:6002.
66. Zhou QF, Zhang Q, Yoshimura T, Trolier-McKinstry S. Appl Phys Lett. 2003; 82:4767.
67. Kari NM, Ritter TA, Park SE, Shrout TR, Shung KK. Proc I EEE Ultrason Symp. 2000; 2:1065.
68. Zhou QF, Cannata JM, Guo HK, Shung KK, Huang CZ, Marmarelis VZ. IEEE Trans Ultrason Ferroelect Freq Contr. 2005; 52:127.
69. Hollenstein E, Davis M, Damjanovic D, Setter N. Appl Phys Lett. 2005; 87:182905.
70. Guo Y, Kakimoto K, Ohsato H. Appl Phys Lett. 2004; 85:4121–3.
71. Zhang GZ, Wang JF, Chen HC, Su WB, Wang CM, Qi P, et al. Appl Phys Lett. 2006; 88:212908.
72. Guo Y, Kakimoto K-i, Ohsato H. Solid State Commun. 2004; 129:279–84.

NIH-PA Author Manuscript NIH-PA Author Manuscript NIH-PA Author Manuscript

73. Chen M, Xu Q, Kim BH, Ahn BK, Ko JH, Kang WJ, et al. J Eur Ceram Soc. 2008; 28:843–9.
74. Xu C, Lin D, Kwok KW. Solid State Sci. 2008; 10:934–40.
75. Chu BJ, Chen DR, Li GR, Yin QR. J Eur Ceram Soc. 2002; 22:2115–22.
76. Oh T, Kim MH. Mater Sci Eng B. 2006; 132:239–46.
77. Zhao S, Li G, Ding A, Wang T, Yin Q. J Phys D: Appl Phys. 2006; 39:2277–81.
78. Lin D, Kowk KW, Chan HLW. Solid State Ionics. 2008; 178:1930–7.
79. Lin DM, Xiao Q, Zhu JG, Yu P. J Eur Ceram Soc. 2006; 26:3247–51.
80. Budd KD, Dey SK, Payne DA. Br Ceram Proc. 1985; 36:107–21.
81. Yi G, Wu Z, Sayer M. J Appl Phys. 1988; 64:2717–24.
82. Tu YL, Calzada ML, Phillips NJ, Milne SJ. J Am Ceram Soc. 1996; 79:441–8.
83. Barrow DA, Petroff TE, Sayer M. Surf Coat Technol. 1995; 76–77:113–8.
84. He, XY.; Ding, AL.; Qiu, PS.; Luo, WG. Proc SPIE in 4th international conference on thin films physics and applications; 2000. p. 609-12.
85. Kholkin AL, Yarmarkin VK, Wu A, Vilarinho PM, Baptista JL. Integr Ferroelectr. 2000; 30:245–52.
86. Barrow DA, Petroff TE, Tandon PR, Sayer M. J Appl Phys. 1997; 81:876–81.
87. Wang Z, Zhou C, Zhu W, Tan OK, Liu W, Yao X. Mater Chem Phys. 2002; 75:71–5.
88. Dorey RA, Whatmore RW. J Eur Ceram Soc. 2004; 24:1091–4.
89. Zhang QQ, Djuth FJ, Zhou QF, Hu C, Cha JH, Shung KK. Ultrasonics. 2006; 44:711–5.
90. Wu DW, Zhou QF, Shung KK, Bharadwaja SSN, Zhang DS, Zhang H. J Am Ceram Soc. 2009; 92(6):1276–9. [PubMed: 20376196]
91. Zhu BP, Han JX, Zhou QF, Shi J, Shung KK, Wei Q, et al. Am Ceram Soc. 2010; 93:2929–31.
92. Akedo J, Lebedev M. Appl Phys Lett. 2000; 77:17101712.
93. Akedo, J.; Levedev, M. Proc. SPIE- nano- and microtechnology: materials, processes packaging and systems; 2002. p. 234-40.
94. Akedo J, Lebedev MS. Jpn J Appl Phys. 2003; 42:5931–5.
95. Akedo JJ. Am Ceram Soc. 2006; 89(6):1834–9.
96. Akedo J, Park JH, Tsuda H. J Electroceram. 2009; 22:319–26.
97. Wang XY, Lee CY, Peng CJ, Chen PY, Chang PZ. Sens Actuat A. 2008; 143:469–74.
98. Lee BS, Lin SC, Wu WJ, Wang XY, Chang PZ, Lee CK. J Micromech Microeng. 2009; 19:065014.
99. Miysoshi T. Jpn J Appl Phys. 2007; 46:7023–108.
100. Hahn DB, Park DS, Choi JJ, Yoon WH, Ryu JH, Kim DY. J Mater Res. 2008; 23:226–35.
101. Choi JJ, Hahn BD, Ryu J, Yoon WH, Park DS. J Appl Phys. 2007; 102:044101.
102. Hahn DB, Kin KH, Park DS, Choi JJ, Ryu JH, Yoon WH, et al. Jpn J Appl Phys. 2008; 47:5545–52.
103. Ryu JH, Choi JJ, Hahn DB, Park DS, Yoon WH, Kim KH. Appl Phys Lett. 2007; 90:152901.
104. Lin D, Kwok KW, Lam KH, Chan HLW. J Appl Phys. 2007; 101:074111.
105. Ryu JH, Choi JJ, Hahn BD, Park DS, Yoon WH. Appl Phys Lett. 2008; 92:012905.
106. Lau, ST.; Li, X.; Zhou, QF.; Shung, KK.; Ryu, JH. Design and fabrication of HF ultrasonic needle transducer with aerosol-deposited lead film. Presented in 10th annual ultrasonic transducer engineering conference; Los Angeles. April 14–16, 2010.;
107. Choi JJ, Jang JH, Hahn BD, Park DS, Yoon WH, Ryu JH, et al. J Am Ceram Soc. 2007; 90:3389–94.
108. Kajiyoshi K, Ishizawa T, Yoshumura. J Am Ceram Soc. 1991; 74:369–74.
109. Kajiyoshi K, Ishizawa T, Yoshumura. Jpn J Appl Phys. 1990; 30:L120.
110. Shimomura K, Tsurumi T, Ohba Y, Daimon M. Jpn J Appl Phys. 1991; 30:2174–7.
111. Ishikawa M, Kurpsawa M, Endou A, Takeuchi S. Jpn J Appl Phys. 2005; 44:4246–342.
112. Ishikawa M, Kadota Y, Takiquchi N, Hosaka H, Morita T. Jpn J App Phys (Part 2-Lett). 2008; 47:7673–7.

NIH-PA Author Manuscript NIH-PA Author Manuscript NIH-PA Author Manuscript

113. Zhu BP, Zhou QF, Shi J, Shung KK, Takeuchi S. Appl Phys Lett. 2009; 94:102901. [PubMed: 19529788]
114. http://www.ruby.colorado.edu/smyth/min/zincite.html.
115. Ito Y, Kushida K, Sugawara K, Takeuchi H. IEEE Trans Ultrason Ferroelect Freq Contr. 1995; 42:316–24.
116. Martin PM, Good MS, Johnston JW, Posakony WJ, Bond LJ, Crawford SL. Thin Solid Films. 2000; 379:253–8.
117. Kamalasanan MN, Chandra S. Thin Solid Films. 1996; 288:112–5.
118. Paraguay FD, Estrada WL, Acosta DRN, Andrade E, Miki-Yoshida M. Thin Solid Films. 1999; 350:192–7.
119. Sakurai K, Kanehiro M, Nakahara K, Tanabe T, Fujita S, Fujita S. J Cryst Growth. 2000; 209:522–8.
120. Yamamoto T, Shiosaki T, Kawabata A. J Appl Phys. 1980; 51:3113–9.
121. Molarius J, Kaitila J, Pensala T, Ylimlammi M. J Mater Sci. 2003; 14:431–8.
122. Gardeniers JEG, Rittersma ZM, Burger GJ. J Appl Phys. 1998; 83:7844–50.
123. Chandrana C, Kharin N, Vince GD, Roy S, Fleischman AJ. IEEE Trans Ultrason Ferroelect Freq Contr. 2010; 57:1077–85.
124. Fleischman, A.; Modi, R.; Nair, A.; Lockwood, G.; Roy, S. IEEE international micro electro mechanical systems conference; Las Vegas, USA. 2002. p. 300-3.
125. Feng GH, Kim ES, Sharp C, Zhou QF, Shung KK. J Micromech Microeng. 2005; 15:586–90.
126. Feng, GH.; Kim, ES. IEEE international micro electro mechanical systems conference; Kyoto, Japan. 2003. p. 594-7.
127. Zhou QF, Cannata J, Meyer R, Van Tol D, Tadigadapa S, Hughes WJ, et al. IEEE Trans Ultrason Ferroelect Freq Contr. 2005; 52:350–7.
128. Zhou QF, Sharp C, Cannata JM, Shung KK, Feng GH, Kim ES. Appl Phys Lett. 2007; 90:113502.
129. Krimholtz R, Leedom DA, Matthaei GL. Electron Lett. 1970; 6:398.
130. Zinin P, Berezina S, Fei D, Rebinsky D, Lemor R, Weiss E, et al. Proc I EEE Ultrason Symp. 2003:881.
131. Cannata JM, Ritter TA, Chen W, Silverman RH, Shung KK. IEEE Trans Ultrason Ferroelect Freq Contr. 2003; 50(11):1548–51.
132. Wang H, Cao W, Zhou QF, Shung KK, Huang YH. Appl Phys Lett. 2004; 85:5998.
133. Lukacs M, Sayer M, Foster FS. IEEE Ultrason Symp. 1997; 2:1709–12.
134. Foster FS, Pavlin CJ, Harasiewicz KA, Christopher DA, Turnbull DH. Ultrasound Med Biol. 2000; 26:1–27. [PubMed: 10687788]
135. Zhu BP, Wu DW, Zhou QF, Shi J, Shung KK. Appl Phys Lett. 2008; 93:012905.
136. Bernstein JJ, Finberg SL, Houston K, Niles LC, Chen HD, Cros LE, et al. IEEE Trans Ultrason Ferroelect Freq Contr. 1997; 44:960–9.
137. Dauchy F, Dorey RA. J Electroceram. 2007; 19:383–6.
138. Dann AE, Bennett DB, Singh RS, Lemaire JJ, Grundfest WS, Grundfest WS. Proc SPIE. 2010; 7629:76290R.
139. Wu DW, Zhou QF, Geng X, Liu CG, Djuth F, Shung KK. IEEE Trans Ultrason Ferroelectr Freq Contr. 2009; 25:2304–10.
140. DeSilets, CS. PhD dissertation. Stanford University; Stanford, CA: May. 1978 Transducer array suitable for acoustic imaging.
141. Lethiecq M, Feuillard G, Ratsimandresy L, Nguyen-Dinh A, Pardo L, Ricote J, et al. Proc IEEE Ultrason Sypm. 1994:1009–13.
142. Nguyen-Dinh A, Ratsimandresy L, Mauchamp P, Dufait R, Flesch A, Lethiecq M. Proc IEEE Ultrason Symp. 1996:943–7.
143. Michau S, Mauchamp P, Dufait R. Proc IEEE Ultrason Symp. 2004:898–901.
144. Ritter, TA.; Gerber, E.; Shung, KK.; Shrout, TR. Method for manufacture of high freqeuency ultrasound transducers. US Patent. 6 183 578. February 6. 2001

NIH-PA Author Manuscript
NIH-PA Author Manuscript
NIH-PA Author Manuscript

145. Ritter TA, Shrout TR, Tutwiler T, Shung KK. IEEE Trans Ultrason Ferroelect Freq Contr. 2002; 49(2):217–30.
146. Cannata JM, Williams JA, Zhou QF, Ritter TA, Shung KK. IEEE Trans Ultrason Ferroelect Freq Contr. 2006; 53(1):224–36.
147. Kokaze Y, Kimura I, Endo M, Ueda M, Kikuchi S, Nishioka Y, et al. Jpn J Appl Phys. 2007; 46(1):280–2.
148. Bale M, Palmer R. J Vac Sci Technol. 2001; B19(6):2020–5.
149. Wang S, Li X, Wakabayashi K, Esashi M. J Am Ceram Soc. 1999; 82(5):1339–41.
150. Subasinghe S, Goyal A, Tadigadapa S. Proc SPIE. 2006; 6109:61090D.
151. Marks S, Almerica JP, Gay MK, Celii FG. Integr Ferroelectr. 2003; 59:333–40.
152. Jung J, Lee W. Jpn J Appl Phys. 2001; 40(1):1408–19.
153. Efremov AM, Kim DP, Kim KT, Kim CI. Plasma Chem Plasma Process. 2004; 24(1):13–28.
154. Kang MG, Kim KT, Kim DP, Kim CI. J Kor Phys Soc. 2002; 41(4):445–50.
155. Qifa, Zhou; Dawai, Wu; Changgeng, Liu; Benpeng, Zhu; Frank, Djuth; Kirk, Shung K. IEEE Ultrason Ferroelect Freq Contr. 2010; 7(10):2213–20.
156. Volkan K, Macit O. J Eur Ceram Soc. 2009; 29(6):1157–63.
157. Shen HF, Guo Q, Zhao ZM, Cao GZ. Mater Res Bull. 2009; 44(11):2152–4.
158. Tsaur J, Wang ZJ, Zhang L, Ichiki M, Wan JW, Mededa R. Jpn J Appl Phys. 2002; 41:6664–8.
159. Weiss EC, Anastasiadis R, Pilarczyk G, Lemor RM, Zinin PV. IEEE Ultrason Ferroelect Freq Contr. 2007; 54(11):2257–71.
160. Jakob A, Weiss EC, Knoll T, Bauerfeld F, Hermann J, Lemore R. Proc IEEE Ultrason Symp. 2007:1605–8.
161. Lee JW, The SY, Lee A, Kim HH, Lee CY, Shung KK. Appl Phys Lett. 2009; 95(7):073701.
162. Lee JW, The SY, Lee A, Kim HH, Lee CY, Shung KK. Ultrasound Med Biol. 2010; 36(2):350–5. [PubMed: 20045590]
163. Jakob A, Bender N, Knoll T, Lemor R, Zhou Q, Zhu BP, et al. Proc IEEE Ultrason Symp. 2009:1722–5.

NIH-PA Author Manuscript
NIH-PA Author Manuscript
NIH-PA Author Manuscript

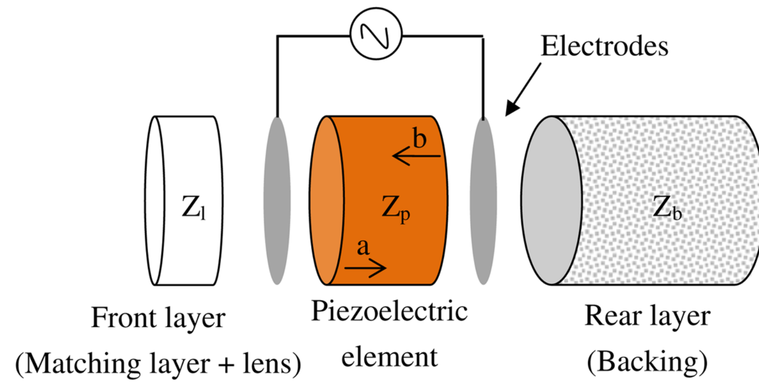

Fig. 1.
Schematic diagram of a single-element piston transducer.

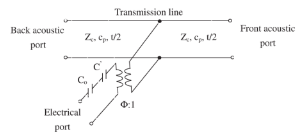

Fig. 2.

KLM electrical equivalent model [24].

NIH-PA Author Manuscript
NIH-PA Author Manuscript

NIH-PA Author Manuscript

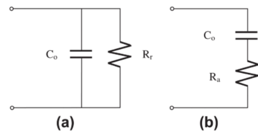

Fig. 3.
Equivalent electrical circuits for a single element transducer near resonance (a) at series resonance and (b) at parallel resonance.

NIH-PA Author Manuscript
NIH-PA Author Manuscript
NIH-PA Author Manuscript

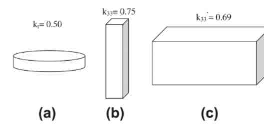

Fig. 4.
The geometry of a piezoelectric material (i.e. PZT-5H) influences its electromechanical coupling coefficient. (a) a circular disc frequently seen in single element transducer; (b) a long bar or pillar frequently used in composite materials; (c) a tall element frequently used in linear arrays.

NIH-PA Author Manuscript
NIH-PA Author Manuscript
NIH-PA Author Manuscript

NIH-PA Author Manuscript

NIH-PA Author Manuscript

NIH-PA Author Manuscript

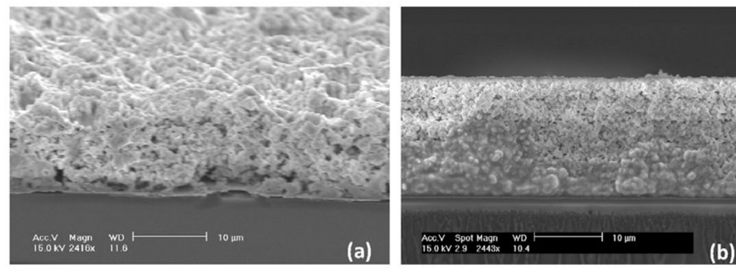

Fig. 5.
SEM cross section of PZT thick film (a) without sol-gel infiltration and (b) with sol-gel infiltration process [89].

NIH-PA Author Manuscript
NIH-PA Author Manuscript
NIH-PA Author Manuscript

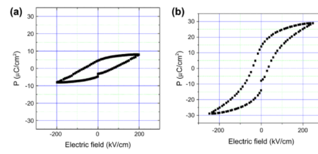

Fig. 6.
P-E loop of PZT thick film: (a) without sol-gel infiltration and (b) with sol-gel infiltration process [89].

NIH-PA Author Manuscript

NIH-PA Author Manuscript

NIH-PA Author Manuscript

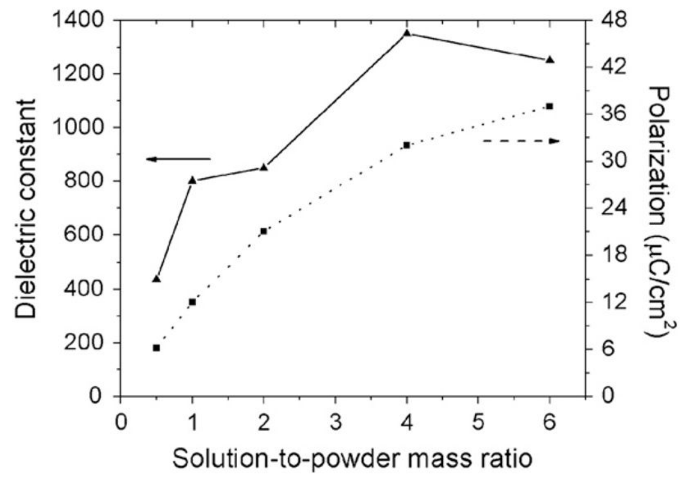

Fig. 7.
Variation of dielectric constant and remnant polarization of the thick films with solution-to-powder mass ratios [90].

NIH-PA Author Manuscript

NIH-PA Author Manuscript

NIH-PA Author Manuscript

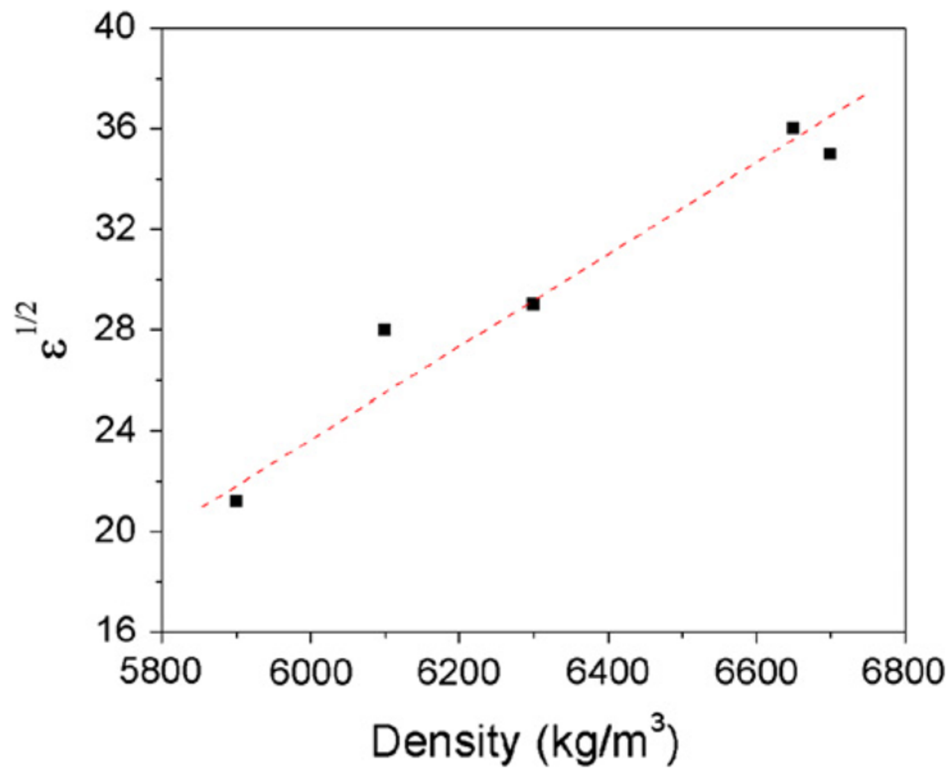

Fig. 8.
Variation of film dielectric constants with film densities. A linear relationship between the square root of the dielectric constants and the densities is observed [90].

NIH-PA Author Manuscript

NIH-PA Author Manuscript

NIH-PA Author Manuscript

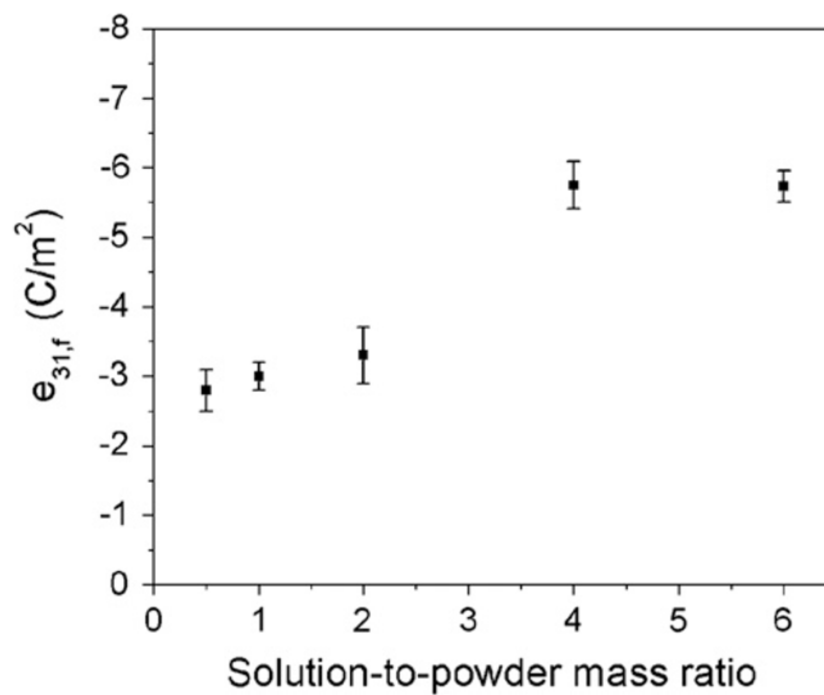

Fig. 9.

Variation of $e_{31,f}$ values with solution-to-powder mass ratio. An increase in $e_{31,f}$ with increasing solution-to-powder mass ratio is observed [90].

NIH-PA Author Manuscript

NIH-PA Author Manuscript

NIH-PA Author Manuscript

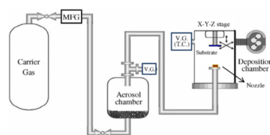

Fig. 10.

Schematic diagram of the setup for the aerosol deposition of piezoelectric thick film [102].

NIH-PA Author Manuscript
NIH-PA Author Manuscript
NIH-PA Author Manuscript

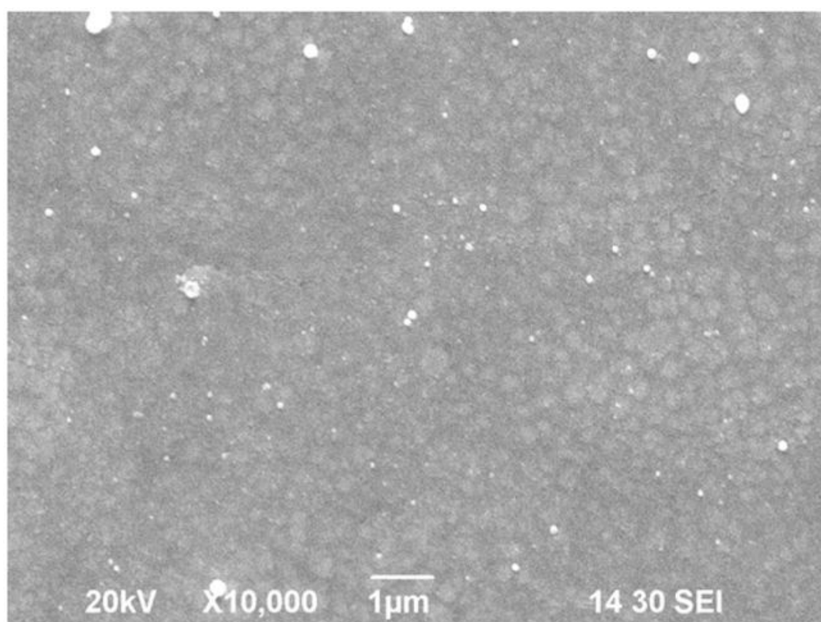

Fig. 11.
FE-SEM micrograph of the KNN–LSO AD film after annealing at ~800 °C for 1 h [106].

NIH-PA Author Manuscript
NIH-PA Author Manuscript
NIH-PA Author Manuscript

Fig. 12.
Components of an autoclave.

NIH-PA Author Manuscript NIH-PA Author Manuscript NIH-PA Author Manuscript

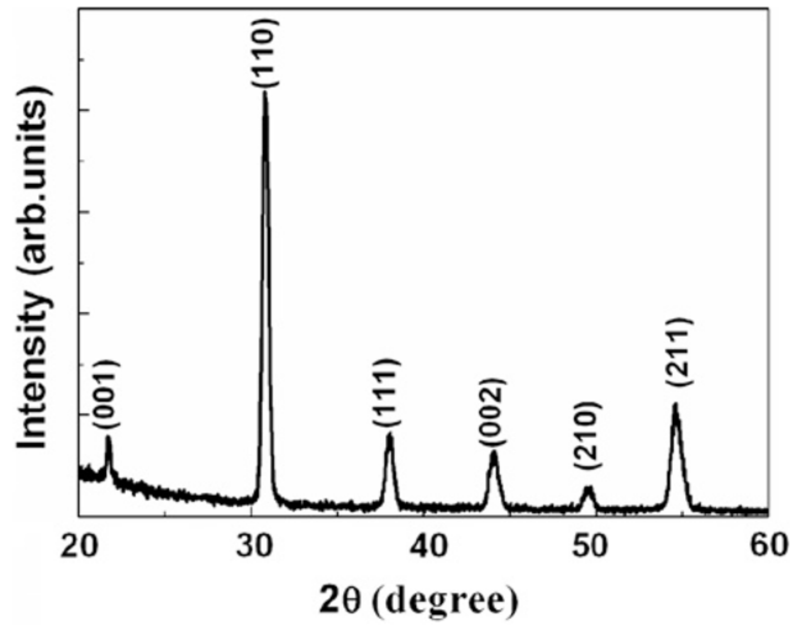

Fig. 13.
XRD pattern of hydrothermal PZT thick films on Ti substrate [113].

NIH-PA Author Manuscript NIH-PA Author Manuscript NIH-PA Author Manuscript

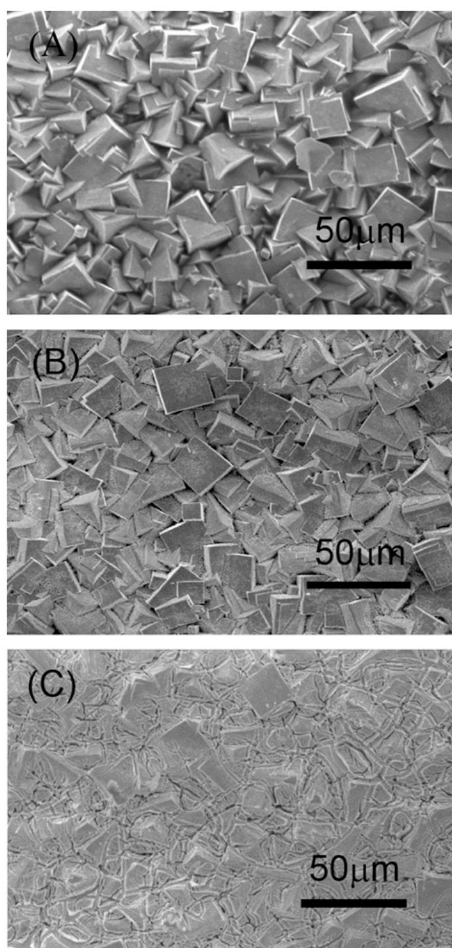

Fig. 14.
SEM surface micrographs of the hydrothermal PZT thick films with different treatments [113].

NIH-PA Author Manuscript

NIH-PA Author Manuscript

NIH-PA Author Manuscript

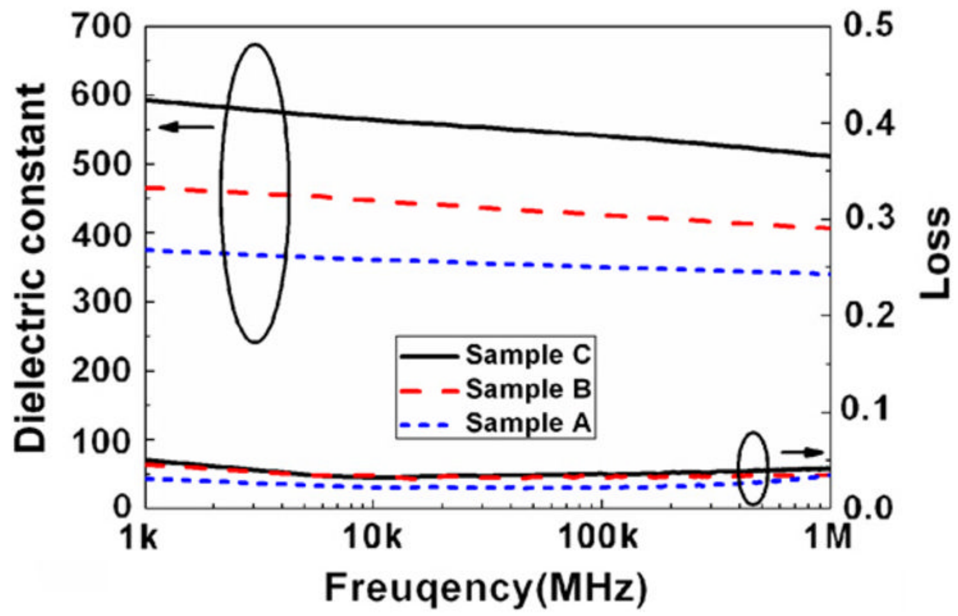

Fig. 15.
Frequency dependence of the dielectric constants and losses of the PZT thick films [113].

NIH-PA Author Manuscript

NIH-PA Author Manuscript

NIH-PA Author Manuscript

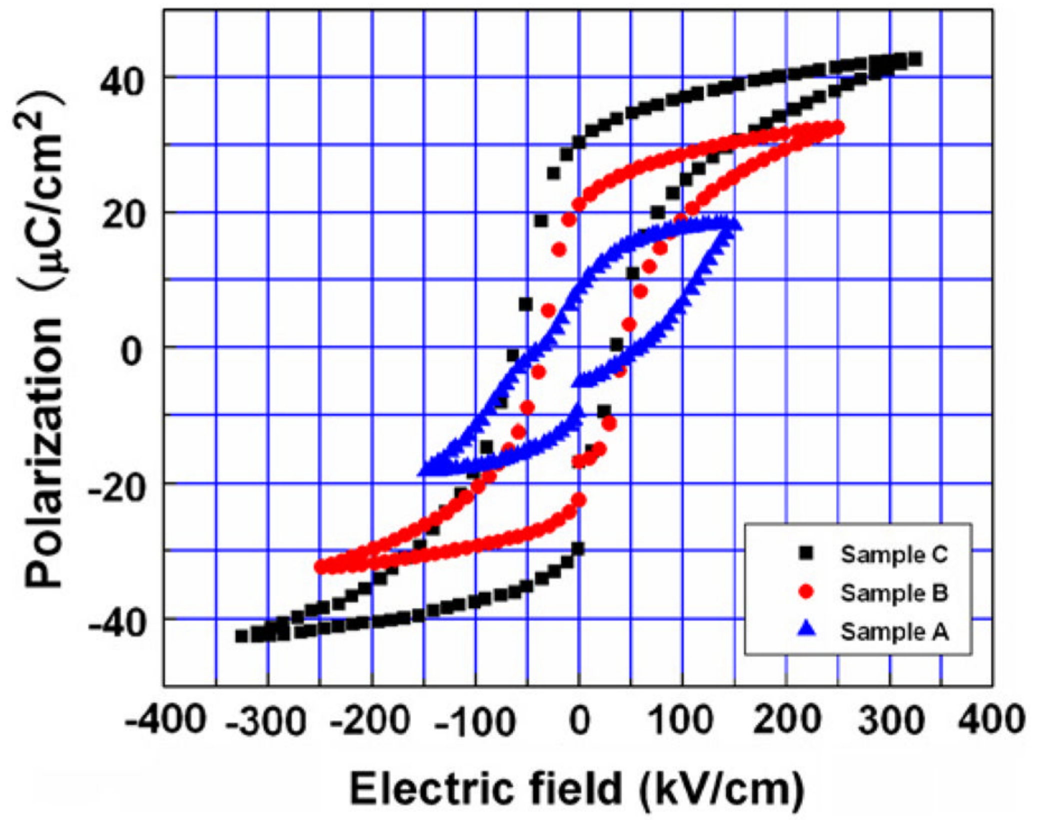

Fig. 16.
Polarization–electric field hysteresis loops of the PZT thick films [113].

NIH-PA Author Manuscript NIH-PA Author Manuscript NIH-PA Author Manuscript

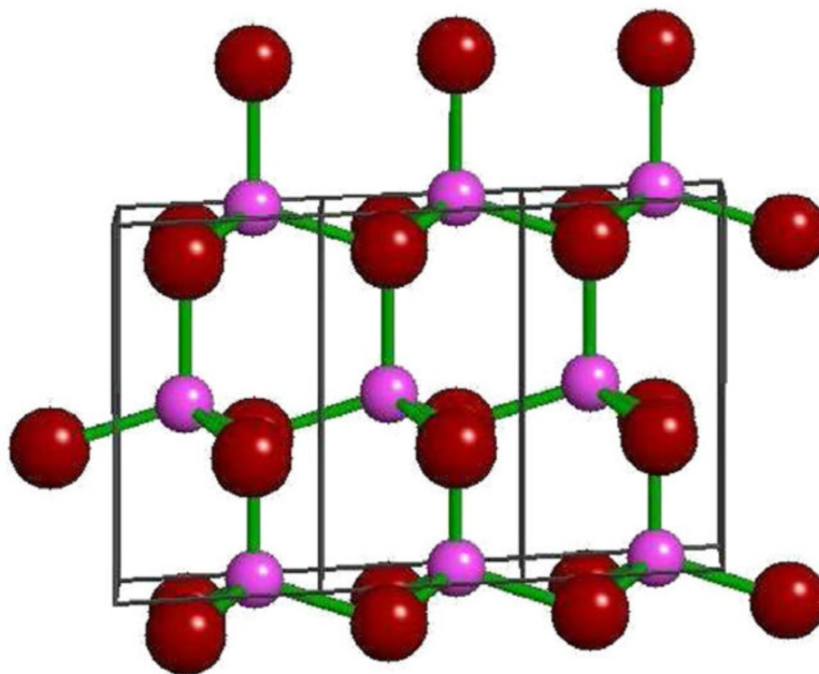

Fig. 17.
The hexagonal wurtzite crystal structure of ZnO. The red atoms are zinc atoms while the purple atoms are oxygen atoms [114].

NIH-PA Author Manuscript
NIH-PA Author Manuscript
NIH-PA Author Manuscript

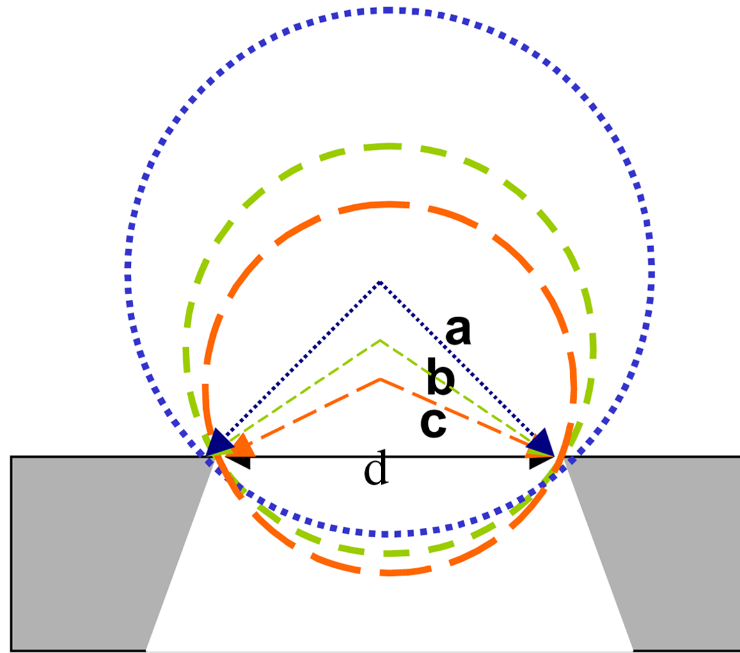

Fig. 18.
Adjustable f-number (F#) design of our fabrication technique [125].

NIH-PA Author Manuscript
NIH-PA Author Manuscript
NIH-PA Author Manuscript

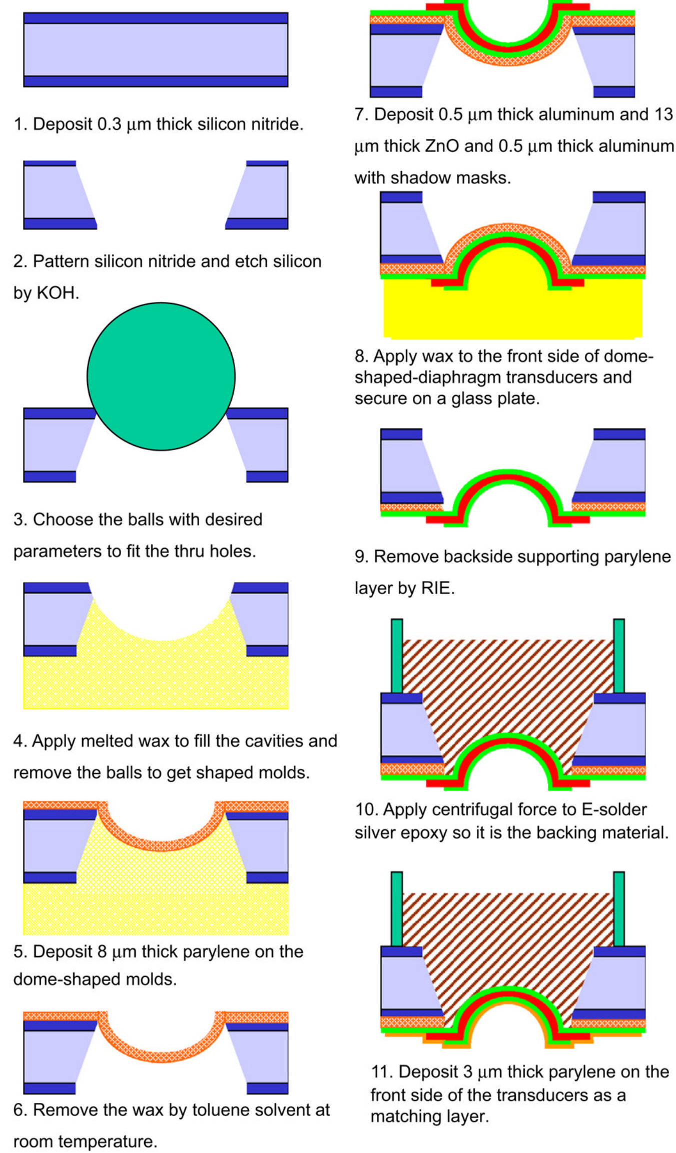

Fig. 19.
pMUT-DSDT fabrication process [125].

NIH-PA Author Manuscript

NIH-PA Author Manuscript

NIH-PA Author Manuscript

Fig. 20.
Shaped wax mold on the silicon substrate [125].

NIH-PA Author Manuscript NIH-PA Author Manuscript NIH-PA Author Manuscript

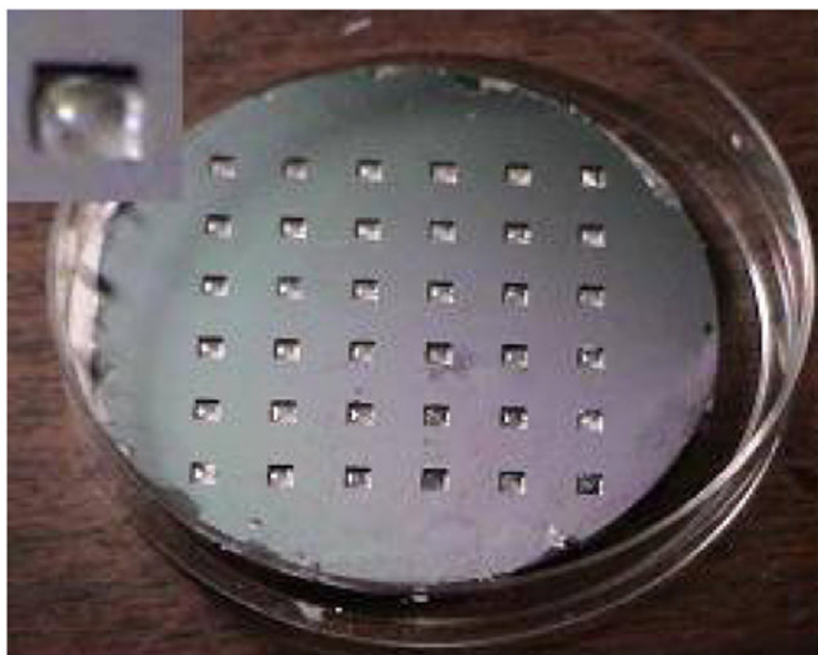

Fig. 21.
Parylene dome-shaped-diaphragms built on silicon substrate [125].

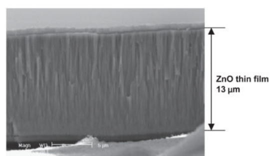

Fig. 22.
SEM photograph of ZnO cross-section [125].

NIH-PA Author Manuscript NIH-PA Author Manuscript NIH-PA Author Manuscript

NIH-PA Author Manuscript
NIH-PA Author Manuscript
NIH-PA Author Manuscript

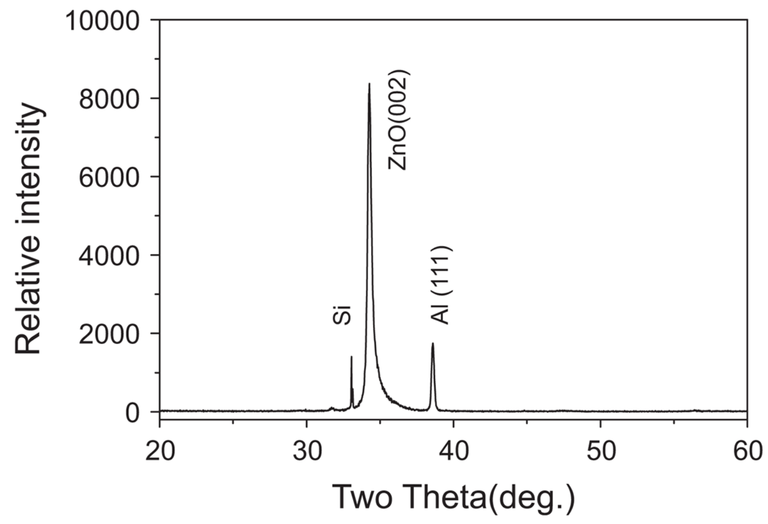

Fig. 23.
XRD patterns of ZnO films deposited on Al electrode/silicon substrate [125].

NIH-PA Author Manuscript NIH-PA Author Manuscript NIH-PA Author Manuscript

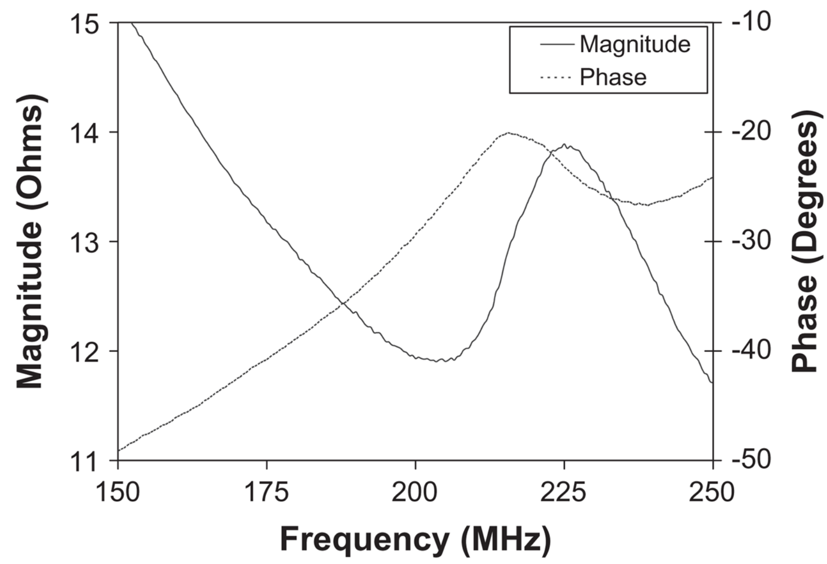

Fig. 24.
Impedance characteristics of the ZnO transducer [125].

NIH-PA Author Manuscript
NIH-PA Author Manuscript
NIH-PA Author Manuscript

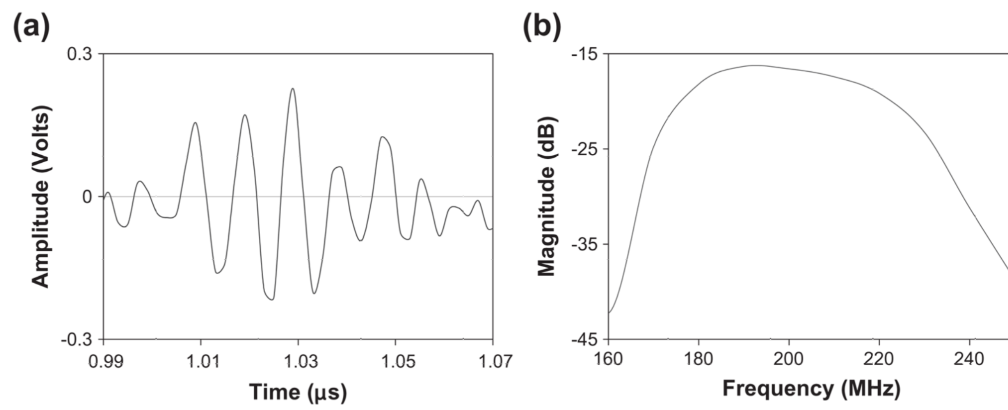

Fig. 25.
Pulse echo waveform received from quartz target (a) and spectrum of the echo response (b) for the ZnO transducer.

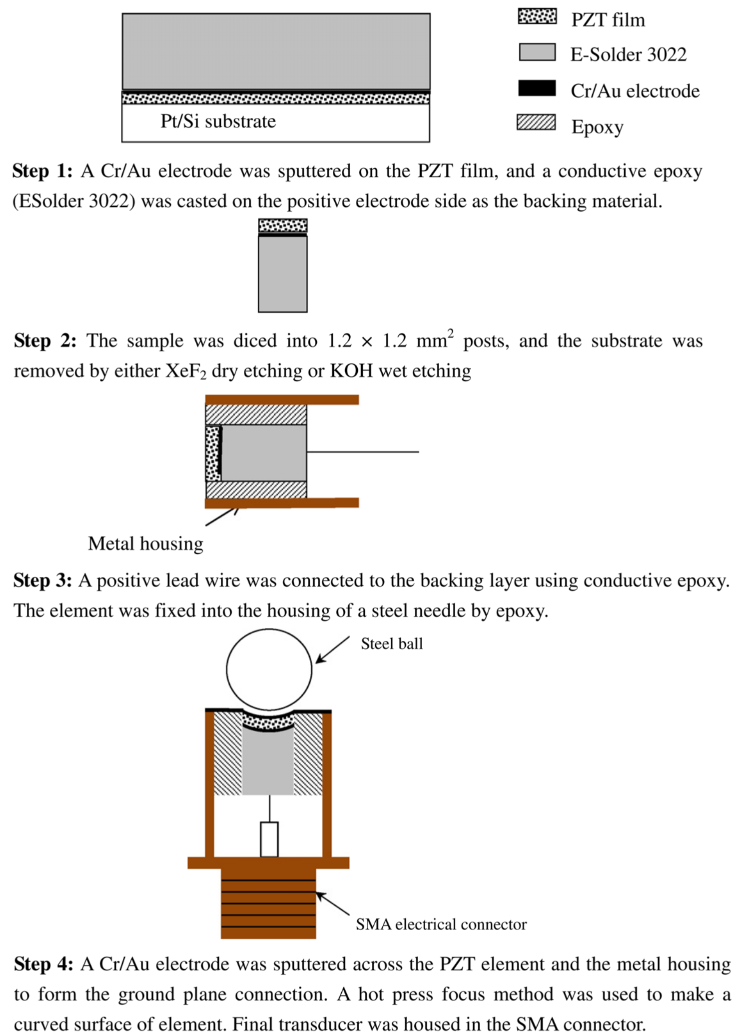

Fig. 26.
Fabrication process of the focus transducer [89].

NIH-PA Author Manuscript NIH-PA Author Manuscript NIH-PA Author Manuscript

NIH-PA Author Manuscript

NIH-PA Author Manuscript

NIH-PA Author Manuscript

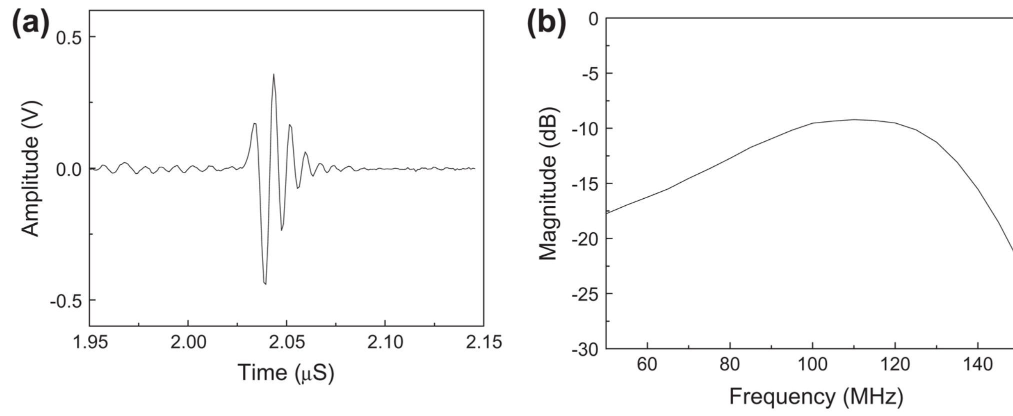

Fig. 27.

Pulse echo of PZT thick film transducer (a) time domain response and (b) Fourier transform spectrum [89].

NIH-PA Author Manuscript

NIH-PA Author Manuscript

NIH-PA Author Manuscript

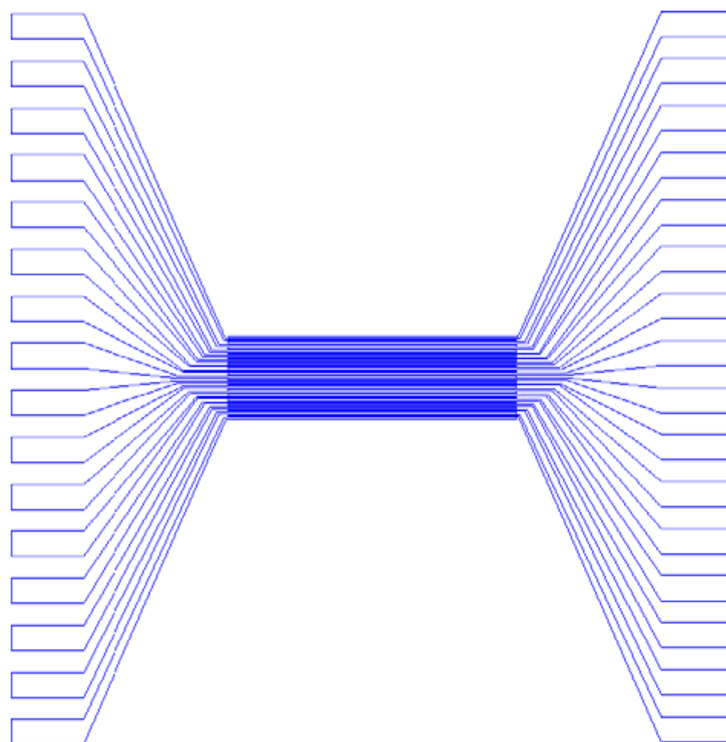

Fig. 28.
Pattern of the array mask.

NIH-PA Author Manuscript

NIH-PA Author Manuscript

NIH-PA Author Manuscript

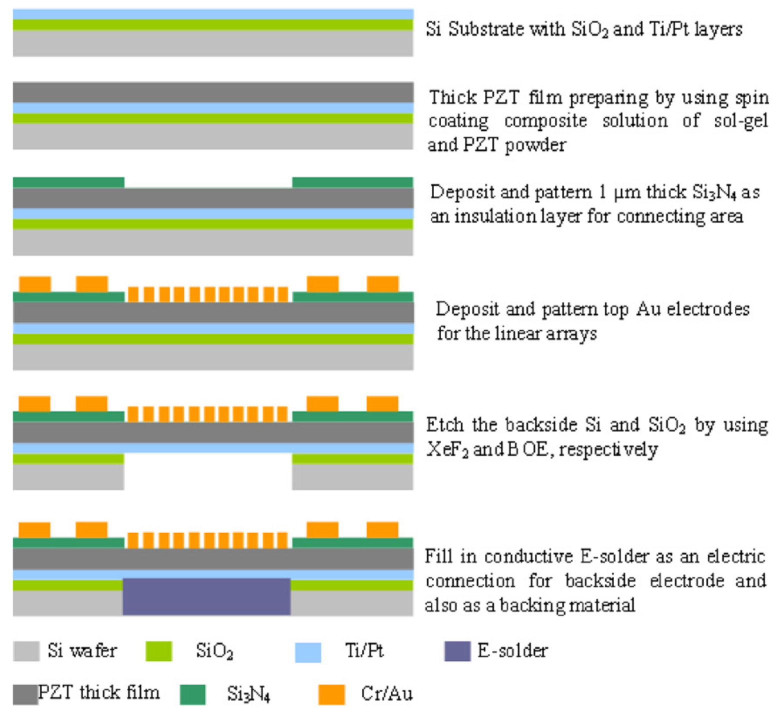

Fig. 29.

Fabrication flow of PZT film kerfless arrays [139].

NIH-PA Author Manuscript

NIH-PA Author Manuscript

NIH-PA Author Manuscript

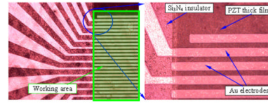

Fig. 30.
Picture of the array pattern with 32 elements [139].

NIH-PA Author Manuscript
NIH-PA Author Manuscript
NIH-PA Author Manuscript

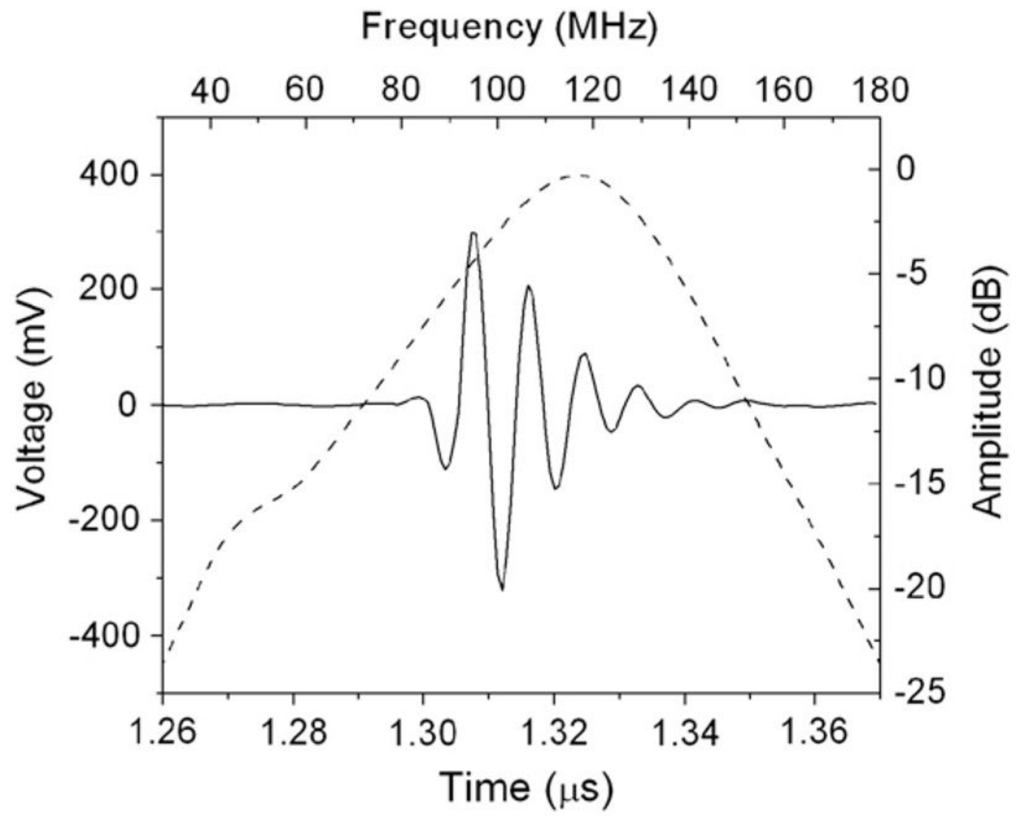

Fig. 31.

Measured pulse-echo signal and frequency spectrum of PZT composite film kerfless array elements [139].

NIH-PA Author Manuscript

NIH-PA Author Manuscript

NIH-PA Author Manuscript

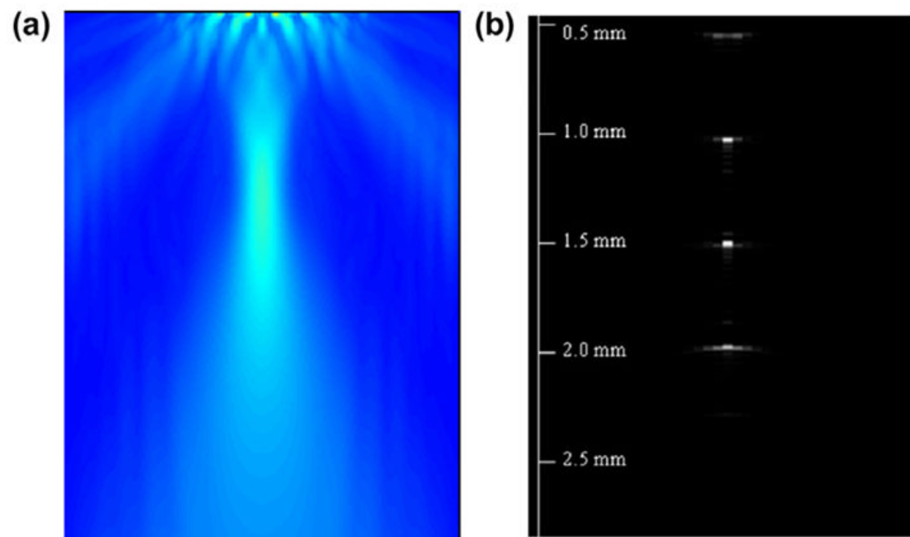

Fig. 32.
(a) Modeled pressure pattern and (b) phantom image of the linear array with PZFLEX and FieldII programs, respectively [155].

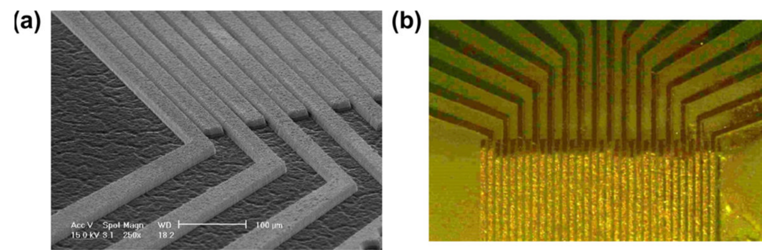

Fig. 33.

Photographs of the linear array dry-etched from a PZT thick film (a) and after epoxy filling (b) [155].

NIH-PA Author Manuscript

NIH-PA Author Manuscript

NIH-PA Author Manuscript

NIH-PA Author Manuscript
NIH-PA Author Manuscript
NIH-PA Author Manuscript

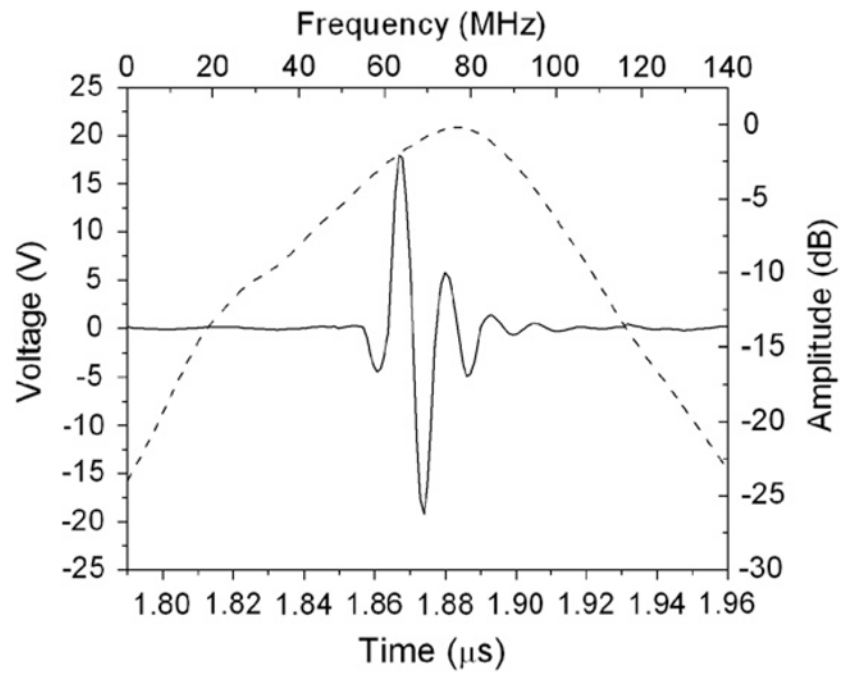

Fig. 34.
Pulse-echo plot and spectrum of a representative array element [155].

NIH-PA Author Manuscript
NIH-PA Author Manuscript
NIH-PA Author Manuscript

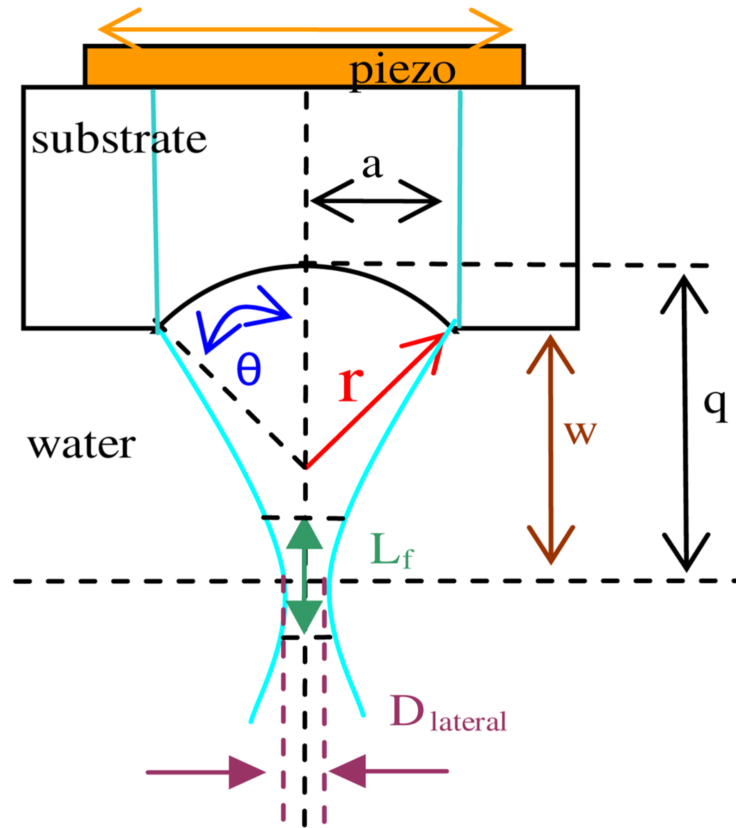

Fig. 35.
Schematic diagram of the silicon-based GHz acoustic lens transducer [163].

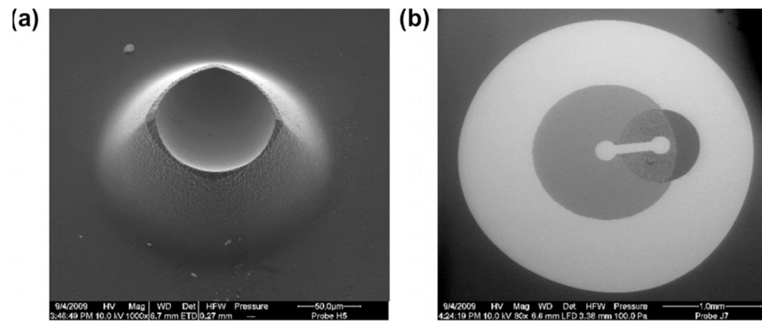

Fig. 36.

REM images of a GHz transducer (a) focusing silicon lens, and (b) piezoelectric layer (ZnO) with electrode [163].

NIH-PA Author Manuscript

NIH-PA Author Manuscript

NIH-PA Author Manuscript

NIH-PA Author Manuscript
NIH-PA Author Manuscript
NIH-PA Author Manuscript

Table 1

Material properties of major piezoelectric materials used in medical ultrasonic transducers.

Property	**PVDF [40,41]**	**PZT-5H [42,43]**	**$PbTiO_3$ [43,44]**	**PMN–PT crystal (33% PT) [45,46]**
d_{33} (pC/N)	−33	593	60	2820
k_t	0.12–0.15	0.51	0.49	0.58
k_{33}	–	0.75	0.51	0.94
$\varepsilon_{33}^{T}/\varepsilon_o$	5–13	1470	180	680–800
c (m/s)	2200	4580	5200	4610
ρ (kg/m^3)	1780	7500	7660	8060
Z_a (MRayl)	3.9	34.4	39.8	37.1
Curie temp. (°C)	100	200	260	130

NIH-PA Author Manuscript NIH-PA Author Manuscript NIH-PA Author Manuscript

Table 2

Material properties of some BNT- and KNN-based lead free ceramics.

System	$\varepsilon_{33}^{S}/\varepsilon_{o}$	d_{33} (10^{-12} C/N)	k_{33}	T_c (°C)	$T_{O\text{–}T}/T_d$ (°C)	Ref.
KNN–Li (7%)	950	240	0.64	460	~20	[69]
KNN–$LiTaO_3$ (5%)	500	235	0.61	460	70	[70]
KNN–$LiSbO_3$ (5%)	1288	283	–	392	45	[71]
KNN–SrTiO3 (0–10%)	412–1448	30–96	–	–	–	[72]
BNT-BT (6–8%, MPB)	601–826	122–176	–	90–105	225–288	[73–76]
BNT-BKT (50%)	825	150	–	320	210	[77]
BNT-6%BT–7.5%Li	990	208	–	85	260	[78,79]

NIH-PA Author Manuscript
NIH-PA Author Manuscript
NIH-PA Author Manuscript

Table 3

Material properties of piezoelectric thick films derived by composite sol–gel technique.

Property	PZT 52/48 [89,90]	Soft-doped PZT [88]	PMN85–PT15/PZT [88]	PMN65–PT35 [91]
$\varepsilon_{33}^{T}/\varepsilon_{o}$	680–1250	900	1800	3326
tan δ	0.040	–	–	0.037
$d_{33,f}$	–	70	59	–
$e_{31,f}$ (C/m^2)	-5.8	-3.4	-5.0	–
P_r (μC/cm^2)	16–37	15	11	30
E_c (kV/cm)	40–43	23	14	100
ρ (kg/m^3)	6500–6700	–	–	–

Table 4

Material properties of piezoelectric thick films derived by aerosol deposition method.

Property	10 µm-PZT 52/48 anneal at 900 °C [102]	50 µm-PZN-PZT anneal at 900 °C [107]	7 µm-KNN–LSO (5.2%) anneal at 800 °C [106]
$\varepsilon_{33}^{T}/\varepsilon_{o}$	1320	1400	1012
tan δ	0.042	0.05	0.07
$d_{33,f}$	150	–	50
P_r (µC/cm^2)	31.1	43.1	15.5
E_c (kV/cm)	26.8	25.2	50

NIH-PA Author Manuscript NIH-PA Author Manuscript NIH-PA Author Manuscript

NIH-PA Author Manuscript NIH-PA Author Manuscript NIH-PA Author Manuscript

Table 5

Performances of the transducers with piezoelectric elements derived by composite sol–gel method and aerosol deposition.

Transducer	f_c (MHz)	−6 dB fractional bandwidth (%)	δ_{axial} (μm)
18 μm composite sol–gel PZT (focus) [89]	103	70	10.3
10 μm composite sol–gel PZT [135]	156	50	9.5
12 μm composite sol–gel PMN–PT [88]	110	64	10.5
6 μm aerosol-deposited KNN–LSO [103]	197	50	7.5